Measurement of the $K^+ \to \pi^+ \nu\bar{\nu}$ branching fraction

A.V. Artamonov,[1] B. Bassalleck,[2] B. Bhuyan,[3, *] E.W. Blackmore,[4] D.A. Bryman,[5] S. Chen,[6, 4] I-H. Chiang,[3]
I.-A. Christidi,[7, †] P.S. Cooper,[8] M.V. Diwan,[3] J.S. Frank,[3] T. Fujiwara,[9] J. Hu,[4] J. Ives,[5] D.E. Jaffe,[3]
S. Kabe,[10] S.H. Kettell,[3] M.M. Khabibullin,[11] A.N. Khotjantsev,[11] P. Kitching,[12] M. Kobayashi,[10]
T.K. Komatsubara,[10] A. Konaka,[4] A.P. Kozhevnikov,[1] Yu.G. Kudenko,[11] A. Kushnirenko,[8, ‡] L.G. Landsberg,[1, §]
B. Lewis,[2] K.K. Li,[3] L.S. Littenberg,[3] J.A. Macdonald,[4, §] J. Mildenberger,[4] O.V. Mineev,[11] M. Miyajima,[13]
K. Mizouchi,[9] V.A. Mukhin,[1] N. Muramatsu,[14] T. Nakano,[14] M. Nomachi,[15] T. Nomura,[9] T. Numao,[4]
V.F. Obraztsov,[1] K. Omata,[10] D.I. Patalakha,[1] S.V. Petrenko,[1] R. Poutissou,[4] E.J. Ramberg,[8] G. Redlinger,[3]
T. Sato,[10] T. Sekiguchi,[10] T. Shinkawa,[16] R.C. Strand,[3] S. Sugimoto,[10] Y. Tamagawa,[13] R. Tschirhart,[8]
T. Tsunemi,[10, ¶] D.V. Vavilov,[1] B. Viren,[3] Zhe Wang,[6, 3] N.V. Yershov,[11] Y. Yoshimura,[10] and T. Yoshioka[10]

(E949 Collaboration)

[1]*Institute for High Energy Physics, Protvino, Moscow Region, 142 280, Russia*
[2]*Department of Physics and Astronomy, University of New Mexico, Albuquerque, NM 87131*
[3]*Brookhaven National Laboratory, Upton, NY 11973*
[4]*TRIUMF, 4004 Wesbrook Mall, Vancouver, British Columbia, Canada V6T 2A3*
[5]*Department of Physics and Astronomy, University of British Columbia, Vancouver, British Columbia, Canada V6T 1Z1*
[6]*Department of Engineering Physics, Tsinghua University, Beijing 100084, China*
[7]*Department of Physics and Astronomy, Stony Brook University, Stony Brook, NY 11794*
[8]*Fermi National Accelerator Laboratory, Batavia, IL 60510*
[9]*Department of Physics, Kyoto University, Sakyo-ku, Kyoto 606-8502, Japan*
[10]*High Energy Accelerator Research Organization (KEK), Oho, Tsukuba, Ibaraki 305-0801, Japan*
[11]*Institute for Nuclear Research RAS, 60 October Revolution Prospect 7a, 117312 Moscow, Russia*
[12]*Centre for Subatomic Research, University of Alberta, Edmonton, Canada T6G 2N5*
[13]*Department of Applied Physics, Fukui University, 3-9-1 Bunkyo, Fukui, Fukui 910-8507, Japan*
[14]*Research Center for Nuclear Physics, Osaka University,*
10-1 Mihogaoka, Ibaraki, Osaka 567-0047, Japan
[15]*Laboratory of Nuclear Studies, Osaka University,*
1-1 Machikaneyama, Toyonaka, Osaka 560-0043, Japan
[16]*Department of Applied Physics, National Defense Academy, Yokosuka, Kanagawa 239-8686, Japan*
(Dated: November 3, 2008)

We have made a remarkable discovery of physics beyond the standard model in the decay $K^+ \to \pi^+ \nu\bar{\nu}$ that will surely change the future of humanity in profound ways. **FIXME: put in the real abstract**

PACS numbers:

I. INTRODUCTION

A. $K^+ \to \pi^+ \nu\bar{\nu}$ in the Standard Model

$K^+ \to \pi^+ \nu\bar{\nu}$ in the Standard Model has been thoroughly discussed in Ref. [1].

B. Other predictions for $K^+ \to \pi^+ \nu\bar{\nu}$

Nearly every model of new physics predicts a deviation from the Standard Model prediction for $K^+ \to \pi^+ \nu\bar{\nu}$. A summary of these current through the first half of 2007 can be found in Buras, Uhlig, and Schwab [2].

C. Interpretation of the decay $K^+ \to \pi^+$ nothing

The only significant Standard Model contribution to $K^+ \to \pi^+$ nothing is $K^+ \to \pi^+ \nu\bar{\nu}$ where $\nu\bar{\nu}$ is $\nu_e\bar{\nu}_e$, $\nu_\mu\bar{\nu}_\mu$ or $\nu_\tau\bar{\nu}_\tau$. Over the years there have been many alternatives suggested, including (i) cases in which the neutrino flavor is not conserved, (ii) those in which neutrinos beyond those in the SM are produced, (iv) those in which a single unseen particle recoils against the π^+ and (iv) more exotic possibilities.

*Now at Department of Physics, Indian Institute of Technology Guwahati, Guwahati, Assam, 781 039, India.
†Now at Physics Department, Aristotle University of Thessaloniki, Thessaloniki 54124, Greece
‡Now at Institute for High Energy Physics, Protvino, Moscow Region, 142 280, Russia.
§Deceased.
¶Now at Department of Physics, Kyoto University, Sakyo-ku, Kyoto 606-8502, Japan.

D. Previous results on $K^+ \rightarrow \pi^+ \nu \bar{\nu}$ below the $K_{\pi 2}$ peak

A detailed discussion of the history of measurements of $K^+ \rightarrow \pi^+ \nu \bar{\nu}$ was given in [1]. However most of these measurements were made in the kinematic region in which the π^+ is more energetic than the π^+ from the background reaction $K^+ \rightarrow \pi^+ \pi^0$ $(K_{\pi 2})$, the so-called '$\pi \nu \bar{\nu}(1)$' region. By contrast very few measurements have been made in the '$\pi \nu \bar{\nu}(2)$' region in which the π^+ is less energetic than that from $K_{\pi 2}$. As will be discussed below, this region is experimentally more problematic than the $\pi \nu \bar{\nu}(1)$ region for a stopped-kaon geometry.

Among the examples of $\pi \nu \bar{\nu}(2)$ measurements was the first attempt to measure $K^+ \rightarrow \pi^+ \nu \bar{\nu}$, a heavy liquid bubble chamber experiment [3][4] at the Argonne Zero Gradient Synchrotron, that was sensitive almost entirely to pion momenta below 200 MeV/c. This experiment achieved a 90% CL limit on the branching ratio of 5.7×10^{-5}, assuming a pure vector spectrum for the π^+. They also extracted limits under the assumptions of tensor and scalar spectra. These were 3.1×10^{-5} and 2.3×10^{-5} respectively.

There followed a series of counter experiments by a Chicago-Berkeley Group that included a measurement in the range 142.7 MeV/$c < p_{\pi^+} < 200.9$ MeV/c [5]. This resulted in a 90% CL upper limit on the branching ratio of 9.4×10^{-7} assuming a vector spectrum. There were also corresponding limits for a tensor spectrum, 7.7×10^{-7}, a scalar spectrum, 1.1×10^{-6} and several other possible shapes.

The next attempt at a measurement in the $\pi \nu \bar{\nu}(2)$ emerged out of the first phase of the E787 experiment [6]. This experiment obtained a 90% CL upper limit of 1.7×10^{-8}, assuming a vector spectrum modified by a form factor obtained from $K^+ \rightarrow \pi^0 e^+ \nu$ data [7]. We henceforth refer to this form as the "Standard Model" interaction. E787 also obtained [8] limits of 1.4×10^{-8} and 2.2×10^{-8} respectively assuming pure tensor and scalar interactions using their $\pi \nu \bar{\nu}(2)$ data exclusively. Adding their $\pi \nu \bar{\nu}(1)$ data [9] they were able to improve these limits to 1.0×10^{-8} and 1.8×10^{-8} respectively

The second generation of this experiment improved the SM limit in the $\pi \nu \bar{\nu}(2)$ region to 4.2×10^{-9}[10] and subsequently to 2.2×10^{-9}[11]. Assuming tensor and scalar interactions this experiment obtained limits of 1.8×10^{-9} and 2.7×10^{-9} respectively [12]

E. The E949 detector

An extensive and detailed description of experiment E949 at Brookhaven National Laboratory has been provided elsewhere [1]. In this Section we provide a summary description of the detector and emphasize the features essential to the acquisition and analysis of data in the $\pi \nu \bar{\nu}(2)$ region.
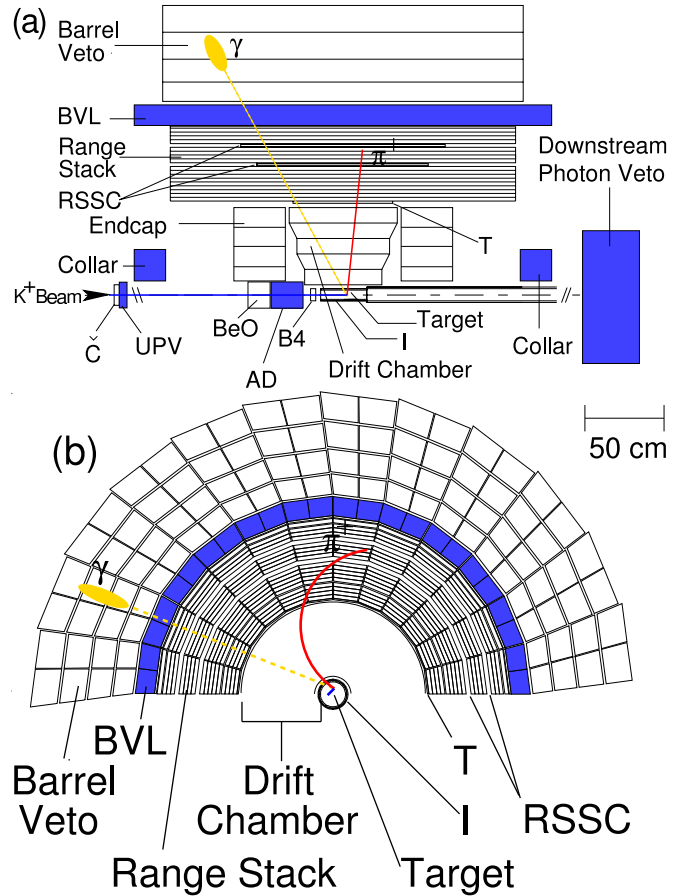
E949 used an incident 710 MeV/c K^+ beam that was

FIG. 1: Schematic side (a) and end (b) views of the upper half of the E949 detector. An incoming K^+ is shown traversing the beam instrumentation, stopping in the target and decaying to $\pi^+ \pi^0$. The outgoing charged pion and one photon from the $\pi^0 \rightarrow \gamma \gamma$ decay are illustrated. Elements of the detector are described in the text.

degraded and stopped in the scintillating fiber target as shown schematically in Figure 1. Observation of the decay $K^+ \rightarrow \pi^+ \nu \bar{\nu}$ requires detection of the incoming K^+ and outgoing π^+ in the absence of any other coincident activity. The charged pion was identified kinematically by energy (E_π), momentum (P_π) and range (R_π) measurements and by observation of the $\pi \rightarrow \mu \rightarrow e$ decay sequence. Since the $K^+ \rightarrow \pi^+ \nu \bar{\nu}$ branching fraction was expected to be at the 10^{-10} level, the detector was designed to have powerful π^+ identification to reject backgrounds from $K^+ \rightarrow \mu^+ \nu_\mu$, $K^+ \rightarrow \mu^+ \nu_\mu \gamma$ and $K^+ \rightarrow \mu^+ \pi^0 \nu_\mu$, photon detection coverage over $4\text{-}\pi$ solid angle to reject $K^+ \rightarrow \pi^+ \pi^0$ and $K^+ \rightarrow \pi^+ \pi^0 \gamma$, and efficient identification of a single incoming K^+ to suppress beam-related background.

E949 employed a right-handed Cartesian coordinate system with $+z$ in the incident beam direction, $+y$ vertically upward and the polar angle θ defined with respect to the $+z$ axis. The entire spectrometer was immersed in a 1 T solenoidal magnetic field in the $+z$ direction.

The incoming charged-particle beam contained ap-

proximately three K^+ for every π^+ and traversed a Čerenkov counter (Č), two beam wire proportional chambers (BWPCs), a passive BeO degrader, an active degrader (AD) and a beam hodoscope (B4) as shown in Figure 1. Typically 1.6×10^6 kaons per second entered the during during a 2.2 s spill. The BWPCs are not explicitly shown in the figure. Čerenkov photons emitted by an incoming K^+ (π^+) passing through a lucite radiator were transmitted (internally reflected) into 14 "kaon" ("pion") photomultiplier tubes (PMTs) to form C_K (C_π) coincidences. The PMT signals are split and fed to analog-to-digital converters (ADCs), time-to-digital converters (TDCs) and amplified by ten and sent to 500 MHz charge-coupled devices (CCDs) [13]. The first (second) BWPC station was located downstream of the Čerenkov counter at 168.5 (68.5) cm from the target entrance. Each BWPC station contained three planes with sense wires in the vertical and $\pm 45°$ to the vertical direction. The wire spacing in the first (second) station was 1.27 (0.80) cm. The BWPCs enabled detection of multiple beam particles. The degraders were designed such that incident kaons stopped in the center of the scintillating fiber target. The AD consisted of 40 layers of 2-mm plastic scintillator (13.9 cm diameter) interleaved with 39 2.2-mm thick copper disks (13.6 cm diameter) azimuthally divided into 12 sectors that were coupled by wavelength-shifting (WLS) fibers to PMTs that were read out by ADCs, TDCs and CCDs. These devices enabled measurement of activity in the AD coincident with the incoming beam and outgoing products of K^+ decays. The B4 hodoscope downstream of the AD had two planes of 16 segmented plastic scintillator counters with 7.2-mm pitch oriented at $\pm 33.5°$ with respect to the horizontal direction. The cross-section of each counter was in a "Z" shape to minimize inactive area seen by the beam and to improve the spatial resolution. Each counter was connected to a PMT by three WLS fibers and each PMT was read out by ADCs, TDCs and CCDs. The B4 enabled a measurement of the target entry position of the beam particle as well as identification of the incident particle by energy loss.

The target was composed of 413 scintillating fibers 3.1-m long with a 5-mm square cross-section packed to form a 12-cm-diameter cylinder. A number of smaller (1-, 2-, and 3.5-mm square) "edge" fibers filled the gaps at the outer edge of the target. Each 5-mm fiber was connected to a PMT and the output PMT signals were split and input into an ADC, TDC, low-gain($\times 1$) and high-gain($\times 3$) CCD. Multiple edge fibers were ganged onto 16 PMTs with similar readout. Analysis of the 500 MHz sampling information provided by the target CCDs was essential for isolating and suppressing backgrounds in the $\pi\nu\bar{\nu}(2)$ region. Two cylindrical layers of six plastic-scintillation counters defined the fiducial volume of the target. The inner layer of counters (dubbed "I counters" or "ICs") were 6.4-mm thick with an inner radius of 6.0 cm and extended 24 cm from the upstream end of the target. The 5-mm thick outer scintillation counters (VC) overlapped

the downstream end of the ICs by 6 mm and extended 196 cm further downstream. The VC served to veto particles that exited the target downstream of the IC. Each IC and VC element was instrumented with a PMT and readout by an ADC, a TDC and a 500 MHz transient digitizer(TD) [14].

The drift chamber, also called the "ultra thin chamber" (UTC) [15], was located just outside the IC and inside the range stack as shown in Figure 1. The UTC extended radially from 7.85 cm to 43.31 cm and served to measure the trajectory and momentum of the charged track from the target to the range stack. Each of the three superlayers of the UTC contains four layers of axial anode wires that provide xy position information between two cathode foil strips that provide z position information. Beginning at an inner radius of 45 cm, the range stack consisted of 19 layers of plastic scintillator counters and staggered double-layer straw chambers (RSSC) embedded after the 10th and 14th layers of scintillator. The range stack enabled the measurement of the range and energy of the charged particle, the observation of the $\pi \to \mu \to e$ decay sequence and the measurement of photon activity. The 19 layers of plastic scintillator counters were azimuthally segmented into 24 sectors as shown in Figure 1. Layers 2-18(19) were 1.9(1.0)-cm thick and 182 cm long and were coupled on both ends to PMTs with lucite light guides. The trigger counters (T counters) in the innermost layer served to define the fiducial volume for K^+ decay products and were 6.4-mm thick and 52-cm long counters coupled to PMTs on both ends by WLS fibers. The T counters were thinner than layers 2-19 to suppress rate due to photon conversions. Signals from each range stack PMT were passively split 1:2:2 for ADCs, discriminators and fan-in modules. The discriminator output was sent to TDCs and used in the trigger. The fanned-in analog sum of 4 PMTs in four adjacent sectors (dubbed a range stack "hextant") was fed into a single TD and provided to the trigger. The TDs sample and digitize the charge in 2 ns intervals with an 8-bit resolution. The 500 MHz sampling was sufficient to resolve a $\pi^+ \to \mu^+$ decay with a 5-ns separation between the stopped pion and the emitted muon.

Identification of $K^+ \to \pi^+\nu\bar{\nu}$ decays required detection of any activity coincident with the charged track. Photons from $K_{\pi 2}$ and radiative kaon decays were detected in a hermetic photon veto system with 4-π sr solid angle coverage as shown in Figure 1. Except for the end caps, all photon veto detectors were lead-scintillator sandwich-style electromagnetic calorimeters. Essentially every scintillation counter in the experiment served as a photon veto detector. The barrel veto (BV) and barrel veto liner (BVL) covered 2/3 of 4-π sr in the barrel outside the range stack with a thickness 14.3 and 2.29 radiation lengths (r.l.) at normal incidence, respectively. The downstream and upstream end caps (EC) consisted of 13.5 r.l. thick undoped cesium iodide crystals and covered approximately 1/3 of 4-π sr [16, 17]. The upstream photon veto (UPV) was 3.1 r.l. thick and was mounted

just downstream of the Čerenkov counter with an inner hole for the beam. The upstream and downstream collar (CO) counters shown in Figure 1 provided approximately 9 r.l. at normal incidence. An additional collar counter (μCO) was installed downstream of the downstream CO between the inner face of the magnet end plate and the target [1]. The downstream photon veto (DPV) provided 7.3 r.l. of coverage downstream of the target, EC and collar. The AD was 6.1 r.l. thick and contributed important photon veto coverage in the poorly instrumented region occupied by the incoming beam.

II. TRIGGER

The trigger system for E949 was designed to select $K^+ \rightarrow \pi^+ \nu\bar{\nu}$ events from the large number of K^+ decays and scattered beam particles by requirements on the π^+ range, evidence of a $\pi^+ \rightarrow \mu^+\nu_\mu$ decay in the range stack, lack of other detector activity at the time of the π^+ and the presence of a K^+ at an appropriately earlier time. The elements and architecture of the two-stage trigger system have been described previously [1]; we describe the features essential for the analysis of $\pi\nu\bar{\nu}(2)$ region.

The logical OR of the following two signal triggers was used for the $\pi\nu\bar{\nu}(2)$ analysis

$$\begin{aligned} \pi\nu\bar{\nu}(1) \equiv \ & KB \cdot DC \cdot (T \cdot 2 \cdot IC) \cdot (6_{ct} + 7_{ct}) \cdot \overline{19_{ct}} \\ & \cdot \overline{zfrf} \cdot L0rr1 \cdot HEX \cdot \overline{(BV + BVL + EC)} \\ & \cdot L1.1 \cdot L1.2 \end{aligned} \quad (1)$$

$$\begin{aligned} \pi\nu\bar{\nu}(2) \equiv \ & KB \cdot DC \cdot (T \cdot 2 \cdot IC) \cdot 3_{ct} \cdot 4_{ct} \cdot 5_{ct} \cdot 6_{ct} \\ & \cdot \overline{(13_{ct} + \cdots 18_{ct})} \cdot \overline{19_{ct}} \cdot L0rr2 \cdot HEX \\ & \cdot \overline{(BV + BVL + EC)} \cdot L1.1 \cdot L1.2 \ . \end{aligned} \quad (2)$$

We collectively refer to the OR of the $\pi\nu\bar{\nu}(1)$ and $\pi\nu\bar{\nu}(2)$ triggers as $\pi\nu\bar{\nu}(1+2)$.

The K^+ beam condition KB required a coincidence of at least 5 C_K counters, the B4 hodoscope and at least 20 MeV of deposited energy in the target. The KB signal served as the beam strobe for the trigger. $T \cdot 2 \cdot IC$ required a coincidence of the first two range stack layers in the same sector with at least one IC to ensure that a charged track exited the target and entered the range stack. The delayed coincidence (DC) required the IC time to be at least 1.5 ns later than the C_K coincidence to select kaon decays at rest. The $\pi\nu\bar{\nu}(1)$ trigger condition $\overline{zfrf}$ required the z position of the charged track to be within the fiducial region of all traversed range stack layers. The "ct" designation refers to the range stack $T \cdot 2$ sector and the next two adjacent sectors that would be traversed by a positively charged particle in the magnetic field. For the $\pi\nu\bar{\nu}(2)$ trigger, the charged track requirements $3_{ct} \cdot 4_{ct} \cdot 5_{ct} \cdot 6_{ct} \cdot \overline{(13_{ct} + \cdots 18_{ct})} \cdot \overline{19_{ct}}$ ensured hits in layers T through 6 to suppress contributions from 3-body K^+ decays and vetoed on hits in the outer layers

to suppress long-range charged tracks beyond the $\pi\nu\bar{\nu}(2)$ kinematic region. The BV, BVL, EC and HEX requirements vetoed events with photons in the BV, BVL, EC and range stack, respectively. The $L0rr1$ and $L0rr2$ were refined requirements of the charged track range taking into account the number of target fibers hit and the track's z position in layers 3, 11, 12, 13 as well as the deepest layer of penetration in order to reject long range tracks such as the μ^+ from $K^+ \rightarrow \mu^+\nu_\mu$ ($K_{\mu 2}$) decay. The $L1.1$ used the ratio of the height and area of the pulse(s) recorded by the TD to select the two-pulse signature of the $\pi^+ \rightarrow \mu^+$ decay in the range stack counter in which the charged track was determined to have stopped. The $L1.2$ used data digitized by the range stack ADCs to reject events with hits near the stopping counter that could falsely satisfy the $L1.1$ and to reject events with hits in both of the two adjacent hextants when the $T \cdot 2$ and stopping counter were in the same sector. For the final 39% of the data taking, an online pion Čerenkov veto was included in the $\pi\nu\bar{\nu}(2)$ trigger due to an increase in the rate of beam pions caused by a beam line malfunction.

In addition to the $\pi\nu\bar{\nu}(2)$ and $\pi\nu\bar{\nu}(1)$ triggers, additional "monitor" triggers were formed for calibration, monitoring, acceptance and background measurements [1]. The monitor triggers used subsets of the components of the signal trigger to predominantly select events due to $K_{\mu 2}$ and $K_{\pi 2}$ decays as well as scattered beam pions (π_{scat}). An additional "CEX" monitor trigger requiring two $T \cdot 2$ hits was used to collect events resulting from the charge-exchange process $K^+ n \rightarrow p K_S^0$ followed by $K_S^0 \rightarrow \pi^+\pi^-$. Information derived from this CEX monitor data was used as input to simulation to determine the background from charge-exchange as described in Section III C 3. In order to measure the efficiency of the $T \cdot 2 \cdot IC$ condition (Section III D), we also defined a KB monitor trigger that required KB condition described previously.

III. DATA ANALYSIS

A. Overview

Identification of the $K^+ \rightarrow \pi^+\nu\bar{\nu}$ decay involved positive observation of the K^+ and daughter π^+ in the absence of coincident detector activity. $K^+ \rightarrow \pi^+\nu\bar{\nu}$ has been studied in two kinematic regions dubbed "$\pi\nu\bar{\nu}(1)$" and "$\pi\nu\bar{\nu}(2)$" that lie above and below the $K_{\pi 2}$ peak, respectively (Figure 2). The $\pi\nu\bar{\nu}(1)$ and $\pi\nu\bar{\nu}(2)$ regions in E949 extended from 211 to 229 MeV/c [1] and 140 to 199 MeV/c in π^+ momentum, respectively. In the $\pi\nu\bar{\nu}(1)$ region, the background was dominated by $K_{\pi 2}$, $K_{\mu 2}$, $K^+ \rightarrow \mu^+\nu_\mu\gamma$ and $K^+ \rightarrow \pi^0\mu^+\nu_\mu$ decays and was sufficiently suppressed by positive identification of the π^+ based on kinematic properties, observation of the $\pi \rightarrow \mu \rightarrow e$ sequence and by the hermetic photon veto capability [1]. Previous studies [11, 18] in $\pi\nu\bar{\nu}(2)$ re-
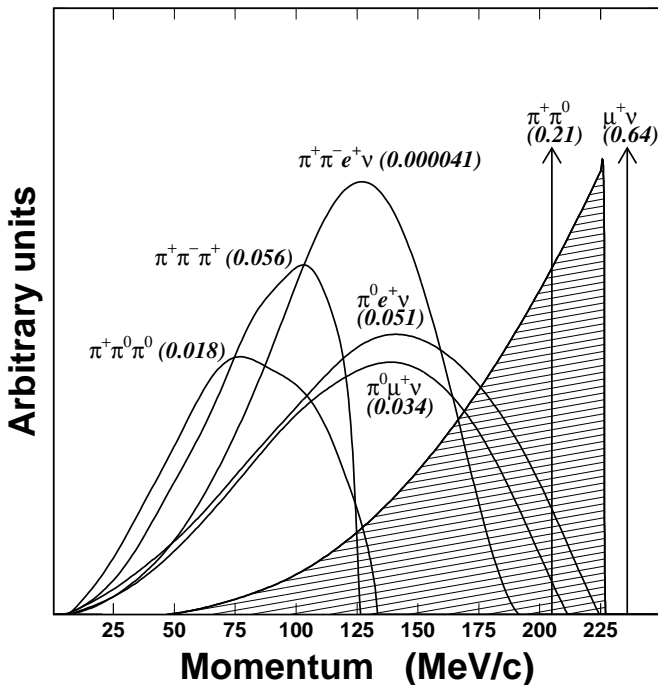
FIG. 2: Momentum spectra of charged particles from K^+ decay in the rest frame. The values in parentheses represent the branching fractions of the decay modes [19]. The hatched spectrum represents the π^+ spectrum from $K^+ \to \pi^+ \nu \bar{\nu}$ decay assuming the $V - A$ interaction.

gion identified the main background as due to $K_{\pi 2}$ decays in which the charged pion scatters in the target, loses energy and falls into the signal region above the $K \to \pi^+ \pi^0 \pi^0$ endpoint and below the $K_{\pi 2}$ peak. Additional lesser sources of kaon decay background with the π^+ in the $\pi \nu \bar{\nu}(2)$ region included $K^+ \to \pi^+ \pi^0 \gamma$ ($K_{\pi 2 \gamma}$) and $K^+ \to \pi^+ \pi^- e + \nu_e$ (K_{e4}). Successful analysis of the $\pi \nu \bar{\nu}(2)$ region relied on the photon veto capability and, in contrast to the $\pi \nu \bar{\nu}(1)$ analysis, identification of the scattering process or the presence of additional particles in the target. The $\pi \nu \bar{\nu}(2)$ region has a larger potential acceptance than $\pi \nu \bar{\nu}(1)$ because the phase space is larger and the loss of π^+ due to nuclear interactions in the detector is smaller at lower pion energies. We also gained acceptance by increasing the size of the signal region with respect to the previous analyses [11, 18] These factors partially mitigated the loss of the acceptance due to these additional requirements needed to suppress background.

1. Kaon decay background

The largest background contribution in the $\pi \nu \bar{\nu}(2)$ region was due to $K_{\pi 2}$ decay in which the charged pion experienced a nuclear interaction near the kaon decay point, probably on a carbon nucleus in the plastic scintillator of the target. The reduced kinetic energy due to the scatter put the pion in the $\pi \nu \bar{\nu}(2)$ region. In addition, the scatter

obscured the directional correlation between the charged and neutral pion, thus directing the photons from π^0 decay away from the barrel region of the photon veto. This background was suppressed by recognition of the scattering process in the target. A smaller background contribution due to scattering of the charged pion in the range stack was suppressed by track pattern and energy deposit in the range stack. The photon veto served to suppress these "$K_{\pi 2}$-scatter" backgrounds as well as background due to the radiative decay $K_{\pi 2 \gamma}$. Background due to K_{e4} was suppressed by identification of additional particles in the target. Kaon decays with a muon in the final state, $K_{\mu 2}$, $K^+ \to \mu^+ \nu_\mu \gamma$ and $K^+ \to \pi^0 \mu^+ \nu_\mu$, were suppressed by kinematics and the recognition of the $\pi \to \mu \to e$ signature as well as the photon veto for the latter two decays.

2. Beam-related background

The beam-related backgrounds were categorized into single- and double-beam background and CEX background. The CEX background occurred due the production of a K^0 in the target due to the charge-exchange process $K^+ n \to p K^0$. If the K^0 turned into a K_L^0 that subsequently underwent semileptonic decay, the π^+ could fall in the $\pi \nu \bar{\nu}(2)$ kinematic region. CEX background was rejected by observing the gap between the K^+ and π^+ fibers due to propagation of the non-ionizing K_L^0, by the inconsistency between the energy deposited by the K^+ and the reconstructed z of the outgoing pion and by identification of the accompanying negative lepton. In addition, requirements on the delayed coincidence between the K^+ and π^+ suppressed CEX background due to the short K_L^0 flight time.

Single-beam background could have been due to a K^+ entering the target and decaying in flight to produce a π^+ in the $\pi \nu \bar{\nu}(2)$ region. Incoming beam π^+, misidentified as K^+, and scattering in the target also contributed to the single-beam background. Positive identification of the incoming particle as a kaon as well as requirements on the delayed coincidence between the incoming and outgoing tracks suppressed the single-beam background.

The two processes that contributed to single-beam background, kaon decay-in-flight and pion scattering, formed the double-beam background when preceded by an additional incoming kaon whose decay products were undetected. Double-beam background was suppressed by requiring a lack of activity in the beam and target in coincidence with the π^+ detected in the range stack.

3. Analysis method and strategy

We used analysis procedures and strategies similar to that of the E949 analysis of the $\pi \nu \bar{\nu}(1)$ region [1] with some extensions that took into account the difficulty of isolating some background samples in the data in the
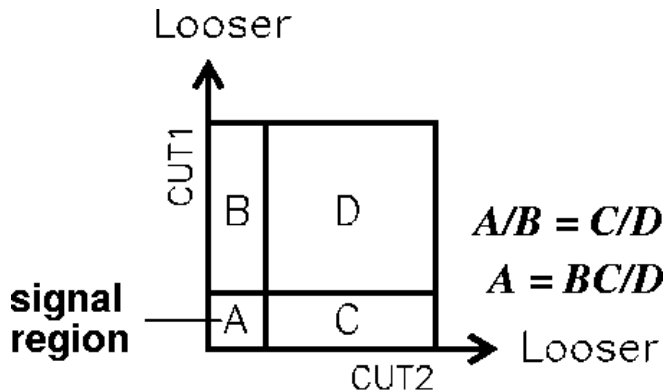
FIG. 3: Schematic of the bifurcation method. The background level in region A can be estimated from the number of events observed in the other regions assuming CUT1 and CUT2 are uncorrelated. See text for details.

$\pi\nu\bar{\nu}(2)$ region. As with the previous analysis, we adopted a "blind" analysis method in that we did not examine the pre-defined signal region until all background and acceptance analysis was completed. Since we also attempted to perform all background estimates directly from the data, we inverted at least one selection criteria ("cut") when we used the $\pi\nu\bar{\nu}(1+2)$ data to avoid examining the signal region. Every third $\pi\nu\bar{\nu}(1+2)$ trigger formed the "1/3" sample that was used to determine the selection criteria. We then obtained unbiased background estimates by applying the finalized selection criteria to the remaining "2/3" sample of $\pi\nu\bar{\nu}(1+2)$ triggers.

The preferred method of background estimation employed the bifurcation method illustrated in Figure 3. The parameter space of two cuts "CUT1" and "CUT2" can be divided into the four regions shown in the figure by the application of each cut or the inverted cut. For example, the number of events in the signal region "A" can be determined by application of both CUT1 and CUT2. If the rejection of CUT1 does not depend on CUT2 and vice versa, then the number of events in A can be estimated as the number of events in region B times the ratio of the number of events in regions C and D or $A = BC/D$. In practice, we employed two branches for the bifurcation analysis. The "normalization branch" analysis was performed to obtain the number of events, $N_{\rm norm}$, in region B. A "rejection branch" analysis was used to obtain D/C. We defined the rejection as $R \equiv (C + D)/C$ and obtained the background estimate as $N_{\rm bkg} = N_{\rm norm}/(R - 1)$. For all background estimates in this analysis, the normalization branch was taken from the $\pi\nu\bar{\nu}(1+2)$ data. We used the $\pi\nu\bar{\nu}(1+2)$ data to obtain the rejection branch for all backgrounds except for the CEX, K_{e4} and $K_{\pi2\gamma}$ backgrounds that could not be cleanly isolated in data. When no events ($N_{\rm norm} = 0$) were available in the normalization branch, we conservatively assigned $N_{\rm norm} = 1$.

We checked the validity of the background estimates by loosening cuts and comparing the predicted the number of events just outside the signal region with observations (Section III C 7). In addition we examined events passing a single major selection criteria to search for unforeseen background sources and coding mistakes (Section III C 8).

B. Data selection requirements

1. Event reconstruction

Events were reconstructed as described in [1] except as noted below. Event reconstruction was performed in a number of steps consisting of track-fitting in various detector systems such as the beam-line detectors, the range stack, the UTC and the target. Multiple iterations of the track-fitting were performed in many of the detector systems using progressively better information from track-fitting from other detector systems as constraints. The following discussion focuses on the target track-fitting to clearly define the target-fiber classification scheme for use in the description of the target CCD fitter and descriptions of the cuts using target fiber information. In contrast to the analysis of the $\pi\nu\bar{\nu}(1)$ region [1], the fit to the UTC track did not include information from the target fibers. Performing the target fit separately improved the ability to detect a pion scatter in or near the target.

After the range stack and UTC track fitting were performed, target fibers were clustered into K^+ and π^+ paths based on geometry, energy and timing information. The pion fibers had to lie along a strip (typically 1 cm in width) along the UTC track extrapolated into the target, have an energy between 0.1 and 10.0 MeV and be in coincidence with the reconstructed time of the π^+ in the range stack (t_{RS}). The kaon fibers had to have greater than 4 MeV of energy and be coincident with the beam strobe. Any fiber that did not fall into the K^+ or π^+ fiber categories was classified as a γ fiber if it had more than 0.1 MeV of energy. The K^+ decay vertex was identified in the K^+ fiber closest to the extrapolated UTC track and farthest from the x-y position of the B4 hit. Pion fibers that were located on the opposite side of the decay vertex with respect to the outgoing track were classified as "opposite-side pion" fibers and were possible due to K^+ decays to multiple charged particles or a photon conversion. The energy-weighted average times of the K^+ and π^+ hits were defined as t_K and t_π, respectively. The sums of the K^+ and π^+ energies were defined as E_K and E_π, respectively.

The identified pion fibers were subjected to a least-squares fit to the hypothesis of positively charged pion track [12]. The "target-track fitter" took into account the x, y positions of each fiber, the consistency with the fitted UTC track, and the observed energy in fibers traversed by the fitted track.

To aid in the identification of pion scattering in the target, the activity in each of the target fibers as recorded by the low-gain and high-gain CCDs (Section I E) was fitted

using a single-pulse and a double-pulse hypothesis. For each channel of each fiber a standardized K^+ pulse used for the target CCD fitter was created using kaon fiber data from $K_{\mu2}$ monitor trigger data. For each fiber having an energy greater than a fiber-dependent threshold, **FIXME: typical threshold?** the fitting procedure was performed on the low-gain and the high-gain CCD information independently. A least-squares fit to the single-pulse hypothesis was attempted for each fiber channel passing the above criteria. The single-pulse fit used two parameters, the pulse amplitude and the time. If the probability of χ^2 ($\mathcal{P}(\chi^2)$) of the single-pulse fit was less than 25%, a double-pulse fit was performed. The double-pulse fit used four parameters, the amplitudes and times for the first and second pulses.

2. Requirements on π^+ in the target

Numerous requirements were placed on the activity in the target to suppress background and ensure reliable determination of the kinematic properties of the charged pion. These requirements were based on the results of the target CCD fitter, the reconstructed energy and time of the pion and kaon fibers, the pattern of kaon and pion fibers relative to information from the rest of the detector and the results of the target-track fitter.

Target pulse data analysis

Detection of pion scattering in the target in the identified kaon fibers required reliable results from the target CCD fitter. For each kaon fiber, the fit results for the high-gain and low-gain channels were examined to determine if $\mathcal{P}(\chi^2) > 5 \times 10^{-5}$ for the double-pulse hypothesis. Next an algorithm determined if the information from the high-gain CCD, the low-gain CCD or a combination of the two should be used for each fiber with an acceptable double-pulse fit. The algorithm was based on the energy in the kaon fiber as measured by the ADC and by the time difference $t_\pi - t_K$. If $\mathcal{P}(\chi^2)$ of the fits for both the single- and double-pulse hypotheses was less than 5×10^{-5} in any of the kaon fibers, then the event was rejected. In addition, the fitted time of the first pulse (t_1) was required to be consistent with average time of the kaon fibers. If any kaon fiber failed the requirement $-6 < t_1 - t_K < 7$ ns, then the event was rejected. This requirement was made on the fitted time t_1 of the single-pulse hypotheses if the probability of χ^2 was greater than 25% and on the fitted time t_1 from the double-pulse hypothesis otherwise. The requirement on t_1 rejected events in which the CCD fitter attempted to fit a fluctuation in the tail of the reference pulse to the data pulse or when there was a large second pulse in the fiber being fit and the fitter mistakenly identified it as the first pulse. For events passing these criteria, the second-pulse activity in a K^+ fiber as found by the target CCD fitting was required to be below 1.25 MeV when the fitted second-pulse time t_2 satisfied the coincidence condition $-7.5 \leq t_2 - t_\pi \leq 10$ ns. In the following we refer to these requirements on the CCD pulse fitting as the "CCDPUL" cut.

Kaon fiber timing

The target K^+ fiber hits were required to be consistent with a kaon approaching the K^+ decay vertex. This consistency was checked by tabulating the times of the kaon fiber hits against the distance to the decay vertex in the x-y plane and against the range of the kaon as determined by deposited energy. This requirement removed events in which the kaon decay vertex was incorrectly assigned.

Pion fiber energy

Pion fibers were required to have energies less than 3.0 MeV. This suppressed π^+ target-scatters since the expected mean energy deposited in a π^+ fiber was approximately 1.2 MeV.

The deposited energy assigned to the pion in the target was required to be consistent with that expected for a π^+ using a cut on a likelihood function. The likelihood function was created based on the measured range and energy of the pion in the target and the pion momentum and calibrated using π_{scat} monitor trigger events. In addition, we required that the total energy of the π^+ target fibers to be in the range of 1 to 28 MeV and that the total energy within ± 5.0 ns of t_{rs} in the target edge fibers to be less than 4.0 MeV.

Pattern of kaon and pion fibers

Events with a minimum distance between the closest pair of kaon and pion fibers greater than 0.6 cm, more than one fiber width, were rejected. This cut suppressed the CEX background. A more stringent version of this cut that also required that no γ fibers filled the gap between the kaon and pion fibers was developed to define the normalization branches for the CEX (Section III C 3) and two-beam (Section III C 5) background measurements.

Two conditions were used to enforce consistency between the positions of the target kaon decay vertex, the kaon and pion clusters, and the beam particle in the B4 hodoscope. The first condition required that the distance in the xy-plane between the hit position in the B4 hodoscope and the nearest tip of the kaon fiber cluster be less than 1.8 cm. The kaon cluster tips were defined to be the two kaon fibers farthest apart from each other. The second condition required that the distance in the xy-plane between the kaon decay vertex and the nearest kaon cluster tip was less than 0.7 cm. This requirement suppressed $K_{\pi2}$ target-scatter background when the scattered π^+ did not emerge from the fiber containing the K^+ decay.

The total energy in the target opposite-side pion fibers within 4.0 ns of t_π was required to be less than 1.0 MeV to suppress background due to K_{e4} decays as well as $K_{\pi2}$ scatters. In the following Sections, this cut is referred to as "OPSVETO".

Target-track fitter

The track determined by the target-track fitter was required to be consistent with the information in the target fibers and the fitted UTC track in order to suppress back-

grounds due to pion scattering, CEX, K_{e4} or a second beam particle in the target. For three components χ_5^2, χ_6^2 and χ_7^2 of the χ^2 for the least-squares fit, we required the probability of χ^2 ($\mathcal{P}(\chi_5^2 + \chi_6^2 + \chi_7^2)$) to be greater than 1%. These components were defined as follows:

- χ_5^2 was assigned a contribution for each pion fiber traversed by the track based on the comparison of the observed energy with the expected energy from the calculated range of the track and the track momentum.

- χ_6^2 was assigned a contribution based on the minimum distance between the track and the nearest point of each fiber that was traversed by the track, but had no observed energy. This assignment acted to force the fitted track to go between fibers and thus provided precise position information on the track.

- χ_7^2 was assigned a contribution for pion fibers that were not traversed by the fitted track based on the distance to the nearest corner.

We rejected events if any single pion fiber contributed more than 35 units to χ_5^2 which might indicate a pion scatter in that fiber. We also required the fitted target track to intersect the kaon vertex fiber. The angle between the reconstructed target track and the UTC track was required to be less than 0.01 radian when the range of the π^+ in the target was less than 2.0 cm. In addition the position of the reconstructed π^+ tracks from the target and UTC fits were required to be well-matched at the target edge. Kinks in the target π^+ track were suppressed by requiring that the difference in the distance of the furthest and nearest pion fiber to the center of the fitted helix of the UTC track was less than 0.35 times the pion range in the target.

3. Pion track requirements

Good pion track reconstruction was required based on the χ^2 of UTC track fit. The cut on the χ^2 was dependent on the number of anode and cathode hits assigned to the fitted track as well as on the number of unused anode and cathode hits. The criteria were determined using both π_{scat} and $K_{\pi2}$ monitor trigger data such that the π^+ momentum resolution of 2.3 MeV/c for the $K_{\pi2}$ peak [1] was not degraded.

Additional range-stack quality cuts were placed on the probability of χ^2 of the range-stack track fit and the agreement of the z position of the extrapolated UTC track with the range-stack timing information and, when applicable, the RSSC information. The RSSC was not available for charged pions that stopped in range stack layers 6 through 10 in contrast to the $\pi\nu\bar\nu(1)$ analysis [1].

Kaons that come to rest in the target were required to have energy loss in the B4 hodoscope and the target consistent with the measured K^+ stopping position based on the z position of the extrapolated UTC track. A likelihood function was formed based on these three quantities and calibrated using $K_{\mu2}$ monitor trigger data. The requirement on this "Beam Likelihood" function suppressed $K_{\pi2}$ target-scatter and CEX backgrounds as well as background due to an incoming beam pions that scattered in the target. In addition we required the z of the extrapolated track to be greater than 5 cm from the upstream end of the target **FIXME: Verify 5cm**.

4. Photon veto requirements

Photon veto requirements were fulfilled within a sub-detector when the sum of activity occurring within a time window exceeded an energy threshold. The time window was referenced to t_{RS}, the reconstructed time of the pion in the range stack. The time window and energy threshold was set for the BV, BVL, range stack, EC, EC_{inner} (the inner ring of the upstream EC was considered a separate sub-detector as it had higher accidental rates than the remaining EC elements due to its proximity to the incoming beam), EC_{2nd} (EC energy identified by a double-pulse-finding algorithm using CCD information was treated as a separate sub-detector), target, IC, VC, CO, and μCO by an optimization algorithm described in [1]. The optimization procedure determined the rejection and acceptance as the time window and energy threshold were varied. The optimization goal was to maximize rejection for a given value of acceptance. The acceptance sample used by the optimization procedure was derived from $K_{\mu2}$ monitor trigger data.

The photon veto requirements for the $\pi\nu\bar\nu(1)$ analysis were optimized using the rejection of $K_{\pi2}$ peak events that were the dominant background with photons in the final state. Ideally the $\pi\nu\bar\nu(2)$ photon veto requirements would have been optimized the rejection on a sample of $K_{\pi2}$ target-scatter events; however, given that photon veto rejection needed to be $\mathcal{O}(5000)$, we were unable to prepare such a sample with sufficient statistics, $\mathcal{O}(500000)$ events, needed to avoid biasing the optimization result. In lieu of this sample, we optimized the photon veto requirements for a majority of sub-detectors using a sample of $K_{\pi2}$ peak events and then optimized the requirements for the remaining sub-detectors using multiple samples of $K_{\pi2}$ target-scatter events as described below.

One sample, dubbed the "kink" sample, contained $K_{\pi2}$ target scatters where the π^+ track had a identifiable kink in the $x-y$ projection, and was created by processing every $\pi\nu\bar\nu(1+2)$ event with a target-track reconstruction algorithm which differed from the target-track reconstruction used for signal candidates (Section III B 1). For kink reconstruction, the restrictions on the pion fiber energy were removed as well as the requirement that the pion fibers had to lie within 1 cm of the extrapolated UTC track. A valid kink event was determined if the following criteria was true: (1) the event had at least two pion

fibers that deviated from the UTC extrapolation, (2) at least one of the fibers from (1) must be adjacent to a kaon fiber, (3) the remaining fibers must be conjoined in a relatively straight line and (4) the event must be rejected by the criteria placed on the standard target-track reconstruction. The kink sample was therefore independent of the sample of signal events. The resulting kink sample had 12000 events.

The primary sample of $K_{\pi2}$ target-scatter events was composed of events that failed either the CCDPUL cut (Section III B 2) or the Beam Likelihood cut (Section III B 3). Additional $K_{\pi2}$ target-scatter samples were composed of events failing these cuts or the other target cuts described in Section III B 2. While these samples were not completely independent of one another, they contained different relative populations of π^+ that initially traveled parallel or perpendicular to the beam direction before scattering.

Before beginning the optimization procedure, we applied a cut on the activity in the BV prior to t_{RS} (BV_{early}) because we found that a large energy deposit (> 30 MeV) in the BV prior to the kaon decay would prevent the TDCs from registering activity coincident with t_{RS} [20]. The $\pi\nu\bar{\nu}(1)$ set of parameters as listed in Table VI of [1] was the starting point for the $\pi\nu\bar{\nu}(2)$ optimization that included all sub-detectors except the AD and DPV. A primary and secondary set of parameters were determined for the eleven sub-detectors listed in Table I and had photon veto acceptance factors of 48% and 25%, respectively.

The AD parameters were determined using the kink sample after application of a photon veto with a rejection of approximately 175 with looser settings on the parameters of the other sub-detectors. These AD parameters yielded an additional photon veto rejection of 1.95 ± 0.08 with a 94% acceptance factor [20]. The primary $K_{\pi2}$ target-scatter sample described above was used to optimize the DPV parameters. After application of all other photon veto parameters at the primary setting listed in Table I, the DPV rejection was measured to be 1.13 ± 0.09 with an acceptance factor of 99.99%.

The BVL_{early} cut was devised as a "safety" cut subsequent to the single-cut failure study on the 1/3 sample (Section III C 8). The cut removed potential $K_{\pi2}$ background when both photons from the π^0 decay deposited energy in the same BVL element. Such an occurrence yielded a reconstructed time earlier than t_{RS}, a reconstructed z position near the center of the element and an apparent energy greater than 10 MeV.

The parameters in the primary column in Table I corresponded to the standard photon veto. For the more restrictive photon veto cut described in Section IV A, the OR of the parameters in the primary and secondary columns were applied.

TABLE I: Time window and energy threshold of the primary and secondary photon veto requirements for each sub-detector as described in the text. RS and TG label the range stack and target parameters, respectively. The parameters for the sub-detectors below the double line were optimized separately. BVL_{early} had the additional requirement that reconstructed z position satisfy $|z| < 4$.

	Primary		Secondary	
	Time	Threshold	Time	Threshold
Sub-detector	window (ns)	(MeV)	window (ns)	(MeV)
BV	[-5.7,10.2]	0.2	[-7.5,10.2]	0.7
BVL	[-4.4,10.7]	0.3	[-3.5,10.6]	0.3
RS	[-4.3,4.4]	0.3	[-3.3,7.8]	0.6
EC	[-4.4,8.0]	0.4	[-6.0,9.5]	0.2
EC_{inner}	[-3.7,5.6]	0.2	[-14.0,9.1]	0.2
EC_{2nd}	[-5.7,2.5]	10.6	[-5.7,2.7]	0.2
TG	[-2.7,2.2]	2.0	[-6.6,2.3]	1.7
IC	[-2.0,4.5]	5.0	[-2.9,9.3]	1.4
VC	[-6.6,1.8]	6.8	[-7.5,7.1]	5.0
CO	[-0.1,5.9]	0.6	[-0.8,5.1]	6.0
μCO	[-5.5,2.3]	3.0	[-4.5,3.3]	1.6
BV_{early}	[-35.7,-5.7]	30.0	[-37.5,-7.5]	30.0
AD	[-2.0,8.0]	0.6	[-2.0,8.0]	0.6
DPV	[-5.0,10.0]	0.0	[-5.0,10.0]	0.0
BVL_{early}	[-5.0,-2.0]	10.0	[-5.0,-2.0]	10.0

q

5. Decay pion kinematic requirements

The upper limit of the signal region in range, energy and momentum was increased with respect to the previous $\pi\nu\bar{\nu}(2)$ analyses [11, 18] to be approximately 2.5 standard deviations from the $K_{\pi2}$ peak similar to the approach used for the E949 $\pi\nu\bar{\nu}(1)$ analysis [1]. The lower limits were not changed with respect to the previous $\pi\nu\bar{\nu}(2)$ analyses. The standard signal region was $140 < P_\pi < 199$ MeV/c, $60 < E_\pi < 100.5$ MeV and $12 < R_\pi < 28$ cm.

A tighter kinematic region was defined as a subset of the standard region to further suppress $K_{\pi2}$ and K_{e4} backgrounds. As shown in Figure 6, $K_{\pi2}$ and K_{e4} events were not uniformly distributed in the signal region. The $K_{\pi2}$ target-scatter events were uniformly distributed in the signal region except for a tail near the $K_{\pi2}$ peak. The K_{e4} background peaked around 160 MeV/c as described in Section III C 2 and the accepted $K^+ \to \pi^+\nu\bar{\nu}$ spectrum is monotonically increasing with momentum in the signal region. Based on these observations, the kinematic region that maximizes the signal acceptance while minimizing the total $K_{\pi2}$ and K_{e4} background was $165 < P_\pi < 197$ MeV/c, $72 < E_\pi < 100$ MeV and $17 < R_\pi < 28$ cm.

Process	Background events
$K_{\pi2}$ target-scatter	$0.619 \pm 0.150^{+0.067}_{-0.100}$
$K_{\pi2}$ range-stack-scatter	$0.030 \pm 0.005 \pm 0.004$
$K_{\pi2\gamma}$	$0.076 \pm 0.007 \pm 0.006$
K_{e4}	$0.176 \pm 0.072^{+0.233}_{-0.124}$
Charge-exchange	$0.013 \pm 0.013^{+0.010}_{-0.003}$
Muon	0.011 ± 0.011
Beam	0.001 ± 0.001
Total	$0.927 \pm 0.168^{+0.320}_{-0.237}$

TABLE II: Summary of the estimated number of events in the signal region from each background component. Each component is described in the text.

6. Delayed coincidence requirements

Determining that the incoming K^+ came to rest in the target was accomplished by observing the delay between the outgoing charged track and the incoming particle. This requirement rejected incoming beam pions that scattered in the target as well as the products of K^+ decay-in-flight. The delayed coincidence also served to suppress the CEX background.

For the standard delayed coincidence requirement, the average time of the kaon fiber hits (t_K) had to be at least 3 ns earlier than the average time of the pion fiber hits (t_π). The previous $\pi\nu\bar{\nu}(2)$ analyses [11, 18] used a tighter requirement of $t_\pi - t_K > 6$ ns. The looser requirement in this analysis resulted in a 9% relative acceptance increase. Under certain conditions the resolution on t_K or t_π was degraded, the degraded time resolution was taken into account by adjusting the minimum delayed coincidence allowed. It was tightened to 4 ns when the energy deposit in the target kaon fibers was less than 50 MeV, when the time of any of the individual kaon fiber differed from the average kaon fiber time by more than 2 ns or when the time of an individual target pion fiber differed from the average time of the pion fiber hits by more than 3.5 ns. It was tightened to 5 ns when the difference between t_K and the B4 hodoscope hit time was greater than 1 ns or when t_π was determined using IC hit time because the average time of the pion fiber hits had poor resolution. It was tightened to 6 ns when the difference between t_π and t_{RS} was greater than 1.5 ns.

A tight version of the delayed coincidence with the requirement that $t_\pi - t_K > 6$ ns was used to subdivide the signal region as described in Section IV A.

C. Evaluation of backgrounds

The evaluation of each component of the background is described in this Section. Table II lists the contribution of each component and the total background.

1. $K_{\pi2(\gamma)}$ background

The $K_{\pi2(\gamma)}$ background contained three components: $K_{\pi2}$ target-scatter, $K_{\pi2}$ range-stack-scatter and $K_{\pi2\gamma}$. For a $K_{\pi2}$ event to have appeared in the signal region, the photons from the π^0 decay had to escape detection and the π^+ had to lose energy via scattering or resolution effects such that it fell into the signal phase space. This scattering could happen in the target ($K_{\pi2}$ target-scatter) or in the range stack ($K_{\pi2}$ range-stack-scatter), but the target-scatter component dominated. Since the π^+ from a $K_{\pi2\gamma}$ decay is not monochromatic, the three final-state photons needed to escape detection for this type of event to be a background

The topology of the most problematic type of $K_{\pi2}$ target-scatter was that of a π^+ initially traveling along the same target fibers in which the kaon deposited energy and scattering into the active region of the detector. The first reason that this type of target-scatter was difficult to reject was that some energy deposited in the target by the scattering π^+ occurred in a kaon fiber (Section III B 2) and could not be distinguished from the larger energy deposited by the stopping kaon. The second reason that this type of target-scatter was difficult to reject was a consequence of the back-to-back production of the π^+ and π^0. A π^+ initially traveling along the kaon fibers meant that the π^0 was also traveling parallel to the beam direction and the resulting photons from the π^0 decay were directed at the upstream or downstream ends of the detector where the photon veto was weakest.

In the $K_{\pi2}$ target-scatter background study, the two bifurcation cuts were chosen as the photon veto cuts (CUT1) and the target-quality cuts (CUT2) since both of these could give powerful rejection of the $K_{\pi2}$ target-scatter background. The bifurcation analysis sample was prepared by applying cuts to to remove the contamination from muon, beam and charge exchange events. In the normalization branch, a combination of $K_{\pi2}$ target-scatter, $K_{\pi2}$ range-stack-scatter and $K_{\pi2\gamma}$ events were selected by inverting the photon veto cut ($\overline{\text{CUT1}}$). All target quality cuts (CUT2) were applied to the sample, resulting in 1131 events left in the normalization branch. After corrections for $K_{\pi2}$ range-stack-scatter contamination, $B = 1107.7 \pm 33.8^{+2.9}_{-2.8}$ events remained in the normalization branch, where the first error is statistical and the second error is systematic. The systematic error comes from the systematic error of the range-stack-scatter cuts when correcting the $K_{\pi2}$ normalization branch for $K_{\pi2}$ range-stack-scatter contamination. Corrections for contamination due to $K_{\pi2\gamma}$ contamination are discussed later in this Section.

For the $K_{\pi2}$ target-scatter rejection branch, the $K_{\pi2}$ target-scatters were classified into two non-exclusive categories. The first category, known as "z-scatters", occurred when the π^+ traveled parallel or anti-parallel to the beam direction, scattered in a kaon fiber and into the active region of the detector. The second category, known as "xy-scatters", occurred when the π^+ scattered

outside of the kaon fibers and the scatter was visible in the xy-plane. To measure the rejection of the photon veto for target-scatter events, six classes of $K_{\pi 2}$ target-scatter events were created by applying or inverting various combinations of the requirements on π^+ in the target (Section III B 2) creating samples with varying mixtures of xy-scatter and z-scatter events. The primary $K_{\pi 2}$ target-scatter sample (Section III B 4) was considered to be the richest in z-scatters and was chosen to measure the photon veto rejection, giving 52 621 events for the region C + D. The photon veto cuts (CUT1) were then applied to the remaining $K_{\pi 2}$ target-scatter events, leaving 22 events for the region C for a rejection of $52621/22 = 2392 \pm 510$. The pion momentum distributions of the normalization and rejection branches are shown in Figure 4. The photon veto of the other five classes of target-scatter events was also measured as well as the photon veto rejection of the primary $K_{\pi 2}$ target-scatter sample in the tighter kinematic region (Section III B 5). The range of measured rejection values was used to set the systematic uncertainty in the photon veto rejection on the $K_{\pi 2}$ target-scatters.

For the $K_{\pi 2}$ range-stack-scatter background events, the cuts with the most powerful rejection were the range-stack quality cuts and the photon veto. The $K_{\pi 2}$ range-stack-scatter normalization branch was a modified version of the $K_{\pi 2}$ target-scatter normalization branch, with the range-stack quality cuts inverted instead of being applied before the inversion the PV cut as was done in the $K_{\pi 2}$ target-scatter normalization branch. This sample of 281 events was heavily contaminated with target-scatter events due to the inefficiency of the range-stack-scatter cuts. By exploiting the events remaining at the end of the $K_{\pi 2}$ target-scatter and $K_{\pi 2}$ range-stack-scatter normalization branches and the measured performance of the range-stack quality cuts relative to $K_{\pi 2}$ range-stack-scatter and signal events, it was possible to estimate the number of $K_{\pi 2}$ range-stack-scatter events present in the original $K_{\pi 2}$ target-scatter normalization branch, giving $23.3 \pm 3.5^{+2.9}_{-3.0}$ $K_{\pi 2}$ range-stack-scatter events in region B.

FIXME: Add equation relating TG and RS scatter bkgd?

The photon veto rejection on the $K_{\pi 2}$ range-stack-scatter events should be the same as that for the unscattered $K_{\pi 2}$ peak events as the back-to-back correlation of the π^+ and π^0 was maintained. The $K_{\pi 2}$ range-stack-scatter rejection branch was created by applying all analysis cuts other than the photon veto cut and the signal kinematic cuts. Instead the $K_{\pi 2}$ peak events were selected, creating a sample of $K_{\pi 2}$ events that did not scatter in the target, giving 122 581 events for the region C + D. The PV cuts (CUT1) were then applied to the remaining $K_{\pi 2}$, leaving 106 events in region C.

The $K_{\pi 2\gamma}$ background estimate was performed using a combination of $K_{\pi 2}$ data and simulated $K_{\pi 2\gamma}$ events. Given a measured number of $K_{\pi 2\gamma}$ events in the Kp2-peak (FIXME - define Kp2-peak), the simulated events were used to predict the number of $K_{\pi 2\gamma}$ events that
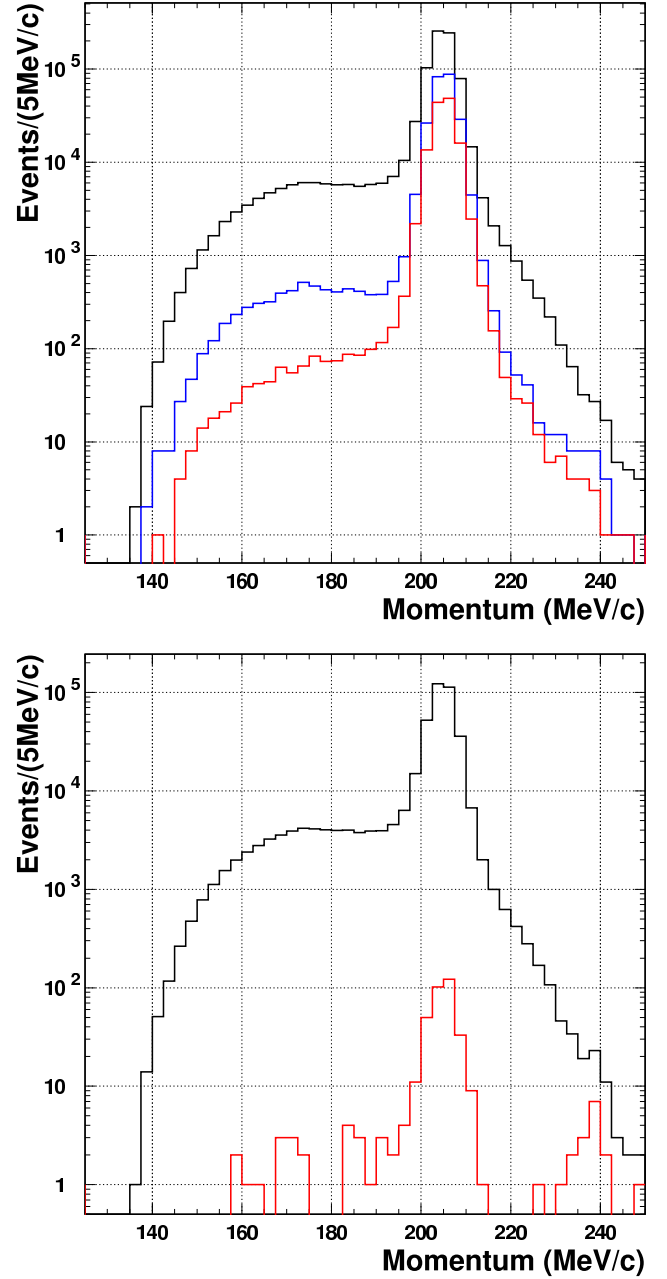

FIG. 4: (Top) Pion momentum distribution for the normalization branch. The black curve represents the distribution after inversion of the photon veto cut. The blue curve shows the suppression of the all the target cuts except for the CCDPUL cut and the red curve shows the suppression of all the target cuts including the CCDPUL cut. (Bottom) Pion momentum distribution of the rejection branch. The events obtained from the inversion of the target cuts is shown in black and the red curve shows the events that survive the photon veto.

would have shown up in the signal region, taking into account the additional photo veto rejection due to the radiative photon. This additional rejection was calculated by combining the distribution of the radiative photon

from simulated events with the single photon detection efficiency as a function of angle and energy from $K_{\pi 2}$ data [21].

The inverted photon veto used to select events for the $K_{\pi 2}$ target-scatter normalization branch would have enhanced the $K_{\pi 2\gamma}$ contamination in this branch due to the presence of the radiative photon. Using $K_{\pi 2}$ monitor triggers it was shown that the $K_{\pi 2}$ target-scatter normalization branch consisted of as much as 30% $K_{\pi 2\gamma}$ events. Based on this upper limit, it was determined that the contributions to the total background due to $K_{\pi 2\gamma}$ events were being entirely double-counted between the $K_{\pi 2\gamma}$ and $K_{\pi 2}$ target-scatter background estimates. To correct for this double-counting the $K_{\pi 2\gamma}$ contribution was subtracted from the $K_{\pi 2}$ target-scatter background. **FIXME: Include estimated background numbers!**

2. K_{e4} background

The $K^+ \to \pi^+\pi^-e^+\nu$ (K_{e4}) decay with a branching ratio of $(4.09 \pm 0.10) \times 10^{-5}$ [19] and a large fraction of the decay π^+ phase space in the kinematic signal region could be a background if the π^- and the e^+ had little kinetic energy and escaped detection in the target. The low energy distribution of the total kinetic energy of the π^- and the e^+ *vs.* the reconstructed π^+ momentum in simulated events shown in Figure 5 indicates where the K_{e4} background would occur kinematically.

Since the main characteristic of K_{e4} event was extra energy in the target from the π^- and the e^+, the target photon veto (TGPV), OPSVETO and CCDPUL cuts were the most effective cuts to suppress this background. Due to contamination by other types of background, such as $K_{\pi 2}$-target-scatter, it was not possible to isolate a pure K_{e4} background sample for a bifurcation analysis using data only. Nonetheless, a K_{e4}-rich sample was selected from data using the CCDPUL $\cdot$ $\overline{\text{TGPV} \cdot \text{OPSVETO}}$ requirement and served as the normalization branch. We established that the majority of the events in the normalization branch were likely to be due to K_{e4} decays by removing the CCDPUL requirement and comparing the momentum distribution of the selected events in the 1/3 sample with the expectation from simulation (Figure 6). In addition, these events were visually examined and determined to be largely due to K_{e4} decays with some contamination from $K_{\pi 2}$ at the 10% level.

Simulated K_{e4} events were used to determine the rejection of the TGPV, OPSVETO, and CCDPUL requirements. Negative pion absorption in the target was modeled based on the energy spectrum of stopped π^- in plastic scintillator observed in E787 [22]. We conservatively assumed that all energy generated from π^- absorption would be promptly deposited in the single fiber where the π^- came to rest. Positron interactions were well-modelled in our EGS4-based simulation [23]. The rejection of the CCDPUL, TGPV and OPSVETO requirements
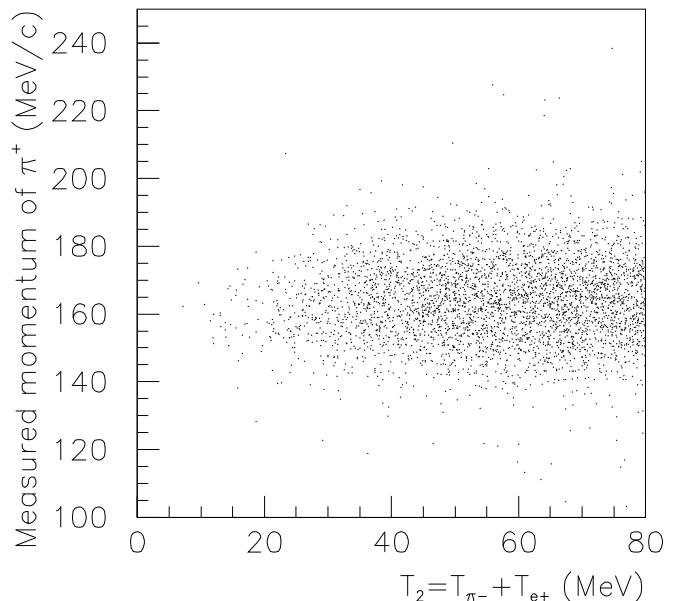

FIG. 5: Total kinetic energy of the π^- and the e^+ versus the measured momentum of the π^+ for simulated K_{e4} events that passed the trigger. **FIXME: abscissa label should be T(pi-) + T(e+)**

were correlated because the target fibers containing the deposited energy of the π^- and e^+ could have been classified as kaon, pion, gamma or opposite-side pion fibers. We used the energy of the simulated deposits to estimate the rejection of these cuts of $R = 52^{+121}_{-29}$. As we did not precisely model either π^- absorption or the inactive material of the the target such as the gaps between the fibers and the cladding and wrapping material of each fiber, we varied the threshold for the energy treated by the CCDPUL (TGPV $\cdot$ OPSVETO) by a factor of 5 (1.5) to estimate the systematic uncertainty associated with the rejection of these cuts. The normalization branch in the 2/3 sample contained 6 events so the K_{e4} background was measured to be $6/(52^{+121}_{-29}-1) \times 1.5 = 0.176 \pm 0.072^{+0.233}_{-0.124}$ where the first error was statistical and the second was systematic.

3. Charge exchange background

Interaction of the incident K^+ in the target was a potential source of background. At low energy, pion production from K^+-nucleon scattering was negligible; however, the charge exchange process (CEX) interaction $K^+n \to K^0p$ could contribute background if the recoil nucleus or proton was not detectable.

When the K^0 decayed as a K^0_S or K^0_L it was a potential background. The delayed coincidence requirement effectively removed any contribution from the short-lived K^0_S. The semileptonic decay processes $K^0_L \to \pi^+e^-\nu_e$ and $K^0_L \to \pi^+\mu^-\nu_\mu$ with branching ratios of 20% and
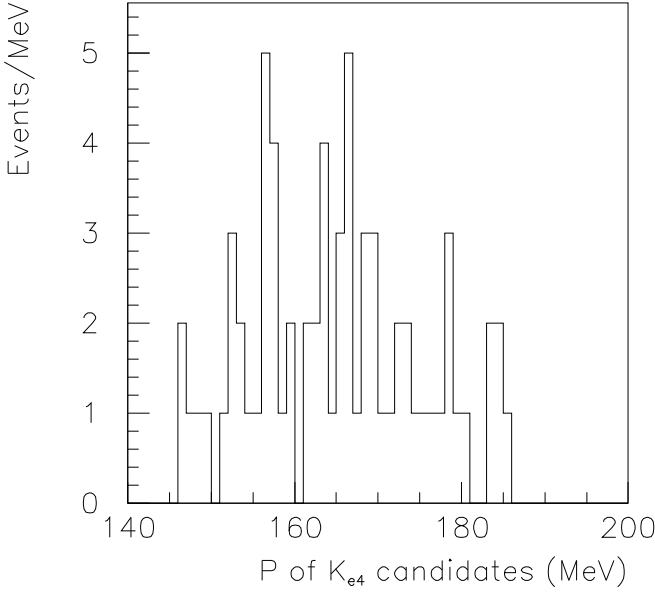
FIG. 6: Momentum distribution of the π^+ in the K_{e4} normalization branch for the 1/3 sample before the application of the CCDPUL cut. **FIXME: Overlay Ke4 from MC with area normalization and Kp2-scat from data with arbitrary normalization. Also MeV should be MeV/c, abscissa label should be 'pi+ momentum'**

FIG. 7: Schematic diagram of the charge exchange process in the target.

K_{e4} (Section III C 2).

14%, respectively, were considered to be the most likely to form a background.

We also considered the possibility of background due to hyperon production where a π^+ was either produced with the hyperon or was a hyperon decay product. Hyperon production would result from $\overline{K^0}$-nucleon interactions if the K^0 oscillated to a $\overline{K^0}$.

Simulation studies showed that there was often a gap between the pion and kaon fibers and that the reconstructed z of the pion track was not consistent with the energy deposited in the kaon fibers as indicated schematically in Figure 7. A CEX-rich sample that served as the normalization branch was selected in $\pi\nu\bar{\nu}(1+2)$ triggers by requiring a gap between the pion and kaon fibers. No target energy cuts were applied in the selection of the normalization sample since the lepton from K_L^0 decay or the π^- and π^0 associated with hyperon production might deposit extra energy in target. The delayed coincidence requirement was also not applied for the normalization sample. The rejection associated with finding a gap in the CEX events, the target energy cuts and the delayed coincidence was determined from simulated CEX events. For the simulation of CEX events, we used reconstructed $K_S^0 \to \pi^+\pi^-$ events obtained from the CEX monitor trigger data (Section II). The reconstructed K_S^0 position and momentum vector were used as the K_L^0 production point and momentum. The background was measured in the 2/3 sample to be $0.013 \pm 0.013(\text{stat.})^{+0.010}_{-0.003}(\text{syst.})$ The systematic uncertainty was estimated by varying the threshold of the target energy cuts analogous to that for
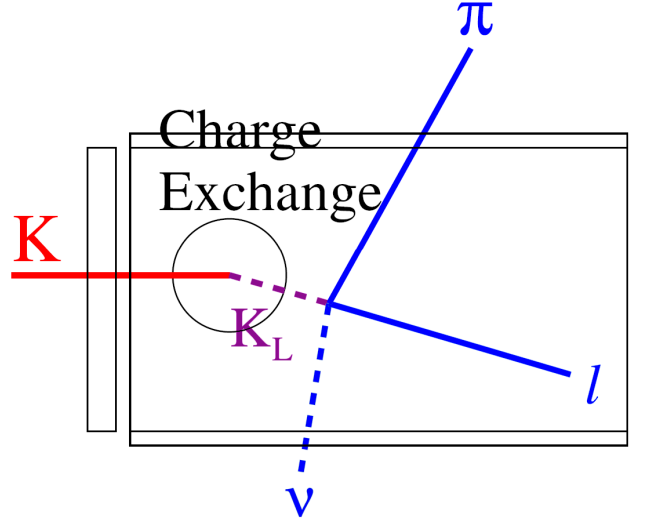
4. Muon background

The decays $K^+ \to \mu^+\nu_\mu$, $K^+ \to \mu^+\nu_\mu\gamma$ and $K^+ \to \mu^+\pi^0\nu_\mu$ could contribute background in the $\pi\nu\bar{\nu}(2)$ kinematic region as indicated in Figure 8. The latter two decays would be background if the photons went undetected and the first decay would be background if the kinematics of the μ^+ were mis-reconstructed. All three processes also required the muon to be mis-identified as a pion in order to be a background.

The two bifurcation cuts were $\pi \to \mu \to e$ identification (CUT1) and the π/μ range-momentum separation (CUT2). The identification of the $\pi \to \mu \to e$ decay chain relied almost entirely on the analysis of the transient digitizer data and will be referred to as the "TD" cut in the following. The normalization branch defined by inverting the TD cut yielded zero events in the 2/3 sample, so N_{norm} was assigned to be unity.

The μ^+ background sample was selected by applying cuts to remove beam backgrounds and a loose version of the photon veto cuts with 95% acceptance to suppress $K_{\pi2}$ backgrounds. To increase statistics the background sample, the kinematic cuts which removed $K_{\mu2}$ peak events were not applied which yielded a sample of with $C + D = 20488$ events in the 2/3 sample. After the application of the TD cut, the number of events remaining were $C = 154$ for a measured TD cut rejection of 133.0 ± 10.7. Thus, the μ^+ background for the was estimated to be 0.0114 ± 0.0114.
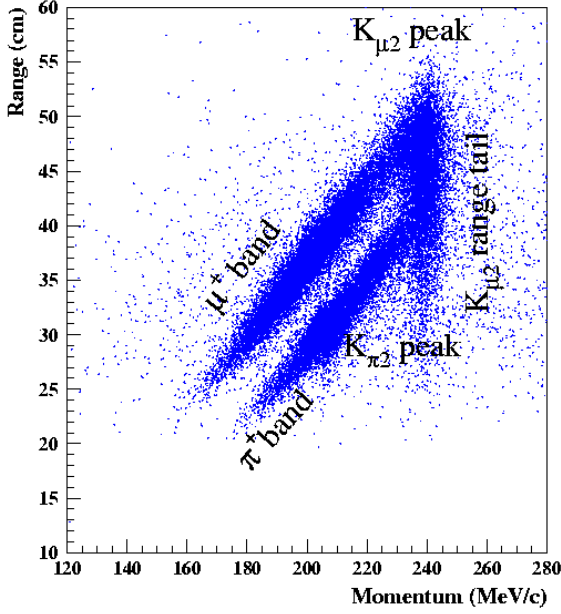
FIG. 8: Pion range *vs.* momentum for $\pi\nu\bar{\nu}(1+2)$ triggers with regions label led as described in the text. **FIXME: PLACE-HOLDER. THIS IS FROM PNN1 PRD PAPER. NEED ANALOGOUS FIGURE FOR PNN1OR2**

5. Beam background

Besides the charge-exchange background discussed in Section III C 3, beam-related background had contributions from a single entering beam particle and two beam particles.

Single-beam background

The bifurcation cuts for single beam background were the delayed coincidence (CUT1) and B4 energy of less than 1.0 MeV (CUT2), which selects beam pions. The sample was selected by applying all the photon veto cuts except TGPV, the kinematic cuts, TD cuts, beam cuts except delayed coincidence, and CUT2. The rejection sample contained $C + D = 12850$ events in the 2/3 data. After the application of the delayed coincidence $C = 2$ events remained for a rejection of the delayed coincidence cut of 6425.0 ± 4542.8. The normalization sample formed by the inversion of the delayed coincidence cut samples yielded zero events, so that N_{norm} was assigned to be 1 ± 1. The measured single beam background was 0.00023 ± 0.00023.

Double-beam background

Double-beam background had two components KK and $K\pi$. For the KK ($K\pi$) background, the decay products of the initial kaon were undetected and a subsequent kaon decay-in-flight (scattered beam pion) provided the outgoing π^+.

FIXME: This section needs to be edited to be consistent with previous sections, etc. Obtaining a KK and $K\pi$ double-beam background sample was done by applying the *tag gaps between K^+ and π^+ tracks* criteria along with inverting the B4 timing cut. From this double beam sample, $K^+ - K^+$ events were obtained by the application of pion Čerenkov cut and by requiring a kaon in the B4 (energy in B4 at t_{rs} be between 1.1 and 5.0 MeV) and $K^+ - \pi^+$ events were obtained by the application of kaon Čerenkov and by requiring a pion in the B4 (B4 energy near t_{rs} be less than 1.1 MeV). The $K^+ - K^+$ ($K^+ - \pi^-$) samples contained $C + D = 1576$ (2467) events. The bifurcation CUT1 was determined to be the following collection of cuts: BW timing, kaon (pion) cerenkov for the $K^+ - K^+$ ($K^+ - \pi^-$) background. Four events remained after applying CUT1 to the rejection sample, $C = 4$ (4).

FIXME: not mentioned in trigger section The $K - \pi$ sample were statistically limited after a change in the $\pi\nu\bar{\nu}(2)$ trigger which added $\overline{C_\pi}$ when the kaon beam contained increased amounts of π^+. Due to this limitation, the $K - \pi$ background was determined within the events before the trigger change and then the background was scaled by the fraction of KB_{live} occurring after the trigger change (2.54). The $K^+ - K^+$ ($K^+ - \pi^-$) normalization sample was obtained by inverting the appropriate CUT1 and contained 2699 (4435) events. The sample was further bifurcated **FIXME: add 2bm bif pic?** where the AD photon veto component was in rejection branch (Rej_{AD}) and the secondary normalization branch applied TG photon veto, target scatter cuts, B4, and target cuts (B'). After the application of the AD photon veto criteria 325 (464) events remained. Thus, the rejection of the AD photon veto on a $K^+ - K^+$ ($K^+ - \pi^-$) sample was 8.30 (9.56). The number of events remaining after the application of the remaining target cuts were 0 for both the $K^+ - K^+$ and $K^+ - \pi^-$ samples, so a value of $B' = 1.0 \pm 1.0$ was used. The corrected $K^+ - K^+$ ($K^+ - \pi^-$) normalization value was determined to be $B = B'/Rej_{AD} = 0.120 \pm 0.120$ (0.105 ± 0.105). The $K - K$ ($K - \pi$) background was measured to be 0.00046 ± 0.00046 (0.00065 ± 0.00065.

6. Background contamination evaluation

Due to the difficulty of isolating background samples in the data, data-driven studies were used to estimate the degree of contamination (i.e., events due to background from other sources) in the $K_{\pi 2}$ target-scatter normalization and rejection branches due to muon and double-beam events. In general contamination of the normalization or rejection branch would result in an overestimate of the background. Bifurcation studies performed in each of these branches limited the contamination to be 1% or less due to muon or double-beam backgrounds. Since the K_{e4} normalization branch was a subset of the $K_{\pi 2}$ target-scatter normalization branch, the K_{e4} contamination in the $K_{\pi 2}$ target-scatter normalization branch was limited to be less than 1%.

FIG. 9: **FIXME: PLACEHOLDER. this will be a custom OTB figure with the PV and CCD cuts as axes and the 3 OTB regions used clearly defined) or target pulse-shape cuts.**

Region	N_E	N_O	$\mathcal{P}(N_O; N_E)$	Combined
CCD_1	$0.79^{+0.46}_{-0.51}$	0	0.45 [0.29,0.62]	
PV_1	$9.09^{+1.53}_{-1.32}$	3	0.02 [0.01,0.05]	0.05 [0.02,0.14]
PV_2	$32.4^{+12.3}_{-8.1}$	34	0.61 [0.05,0.98]	0.14 [0.01,0.40]

TABLE III: Comparison of the expected (N_E) and observed (N_O) number of background events three regions CCD_1, PV_1, and PV_2 outside the signal region. The ventral value of N_E is given along with the combined statistical and systematic uncertainties. $\mathcal{P}(N_O; N_E)$ is the probability of observing N_O or fewer events when N_E events are expected. The rightmost column "Combined" gives the probability of the combined observation in that region and the region(s) of the preceding row(s). The numbers in square brackets are the probabilities reevaluated at the upper and lower bounds of the uncertainty on N_E [24].

7. Background consistency checks

The reliability of the bifurcation method used to estimate the backgrounds relied on the two bifurcation cuts being uncorrelated. Three distinct data regions just outside the signal region were created by loosening the photon veto cut (regions PV_1 and PV_2 in Figure 9) and the CCDPUL cut (region CCD_1 in Figure 9). For uncorrelated cuts the number of observed events should be consistent with the number of events expected in that region using the bifurcation method. The region CCD_1 was the region immediately adjacent to the signal region defined by loosening the pion energy threshold from 1.25 MeV to 2.5 MeV. The region PV_1 was the region immediately adjacent to the signal region defined by loosening the nominal photon veto from an acceptance of 62.0% **FIXME: 48% in pv section** to an acceptance of 89.6% **FIXME: check**. The region PV_2 was the region adjacent to PV_1, bounded by PV_1 and the photon veto used for the $\pi\nu\bar{\nu}(1)$ analysis which had an acceptance of 92.5% **FIXME: check**.

Table III shows the number of expected and observed events as well as the probability of observation. The combined probability of observation of 5% for the two regions nearest the signal region may have indicated that the background was overestimated, but the re-evaluation of this combined probability at the lower limit of the systematic uncertainties [24] gave 14% for the two closest regions which demonstrated that the assigned systematic uncertainties were reasonable.

8. Single-cut failure study

After determination of the selection criteria using the 1/3 data sample, we performed a "single-cut" failure study to identify unexpected sources of background or potential analysis flaws. As the result of this study on the 1/3 data sample, four events revealed evidence of two potential analysis flaws.

Three of the events not rejected by the photon veto cuts showed evidence of a large energy deposit in the BVL. These events were shown to be due to $K_{\pi 2}$ decays in which both photons from the π^0 decay deposited energy in the same BVL counter [21]. The simultaneous activity at each end of a BVL element led to an erroneous average time prior to t_{RS} that was outside the veto time window. A "safety" cut, described in Section III B 4, was devised to remove these events.

The remaining event of the four failed only the photon veto criteria in the AD and revealed a potential flaw in the CCDPUL target-pulse fitting algorithm when the fitted time of the first pulse was inconsistent with the average kaon fiber time. The inconsistency arose when the fitting algorithm incorrectly assigned the first pulse time to an actual second pulse because the second pulse energy was large compared to the first pulse energy. The CCDPUL timing criteria described in Section III B 2 were developed to remove the analysis flaw.

D. Acceptance and sensitivity

We assessed the acceptance of the selection criteria by dividing the criteria into components that could be measured separately using monitor triggers or simulated data. Simulated data were used to estimate the acceptance of trigger and decay phase space as well as to assess the impact of nuclear interactions.

Acceptance factors from $K_{\mu 2}$ events

$K_{\mu 2}$ monitor triggers were used to assess the components of the acceptance regarding the kaon beam, the charged track and the event topology. The acceptance factors are listed in Table IV and described below.

To measure the acceptance of the range stack track reconstruction, a sample of $K_{\mu 2}$ monitor triggers was selected by requiring a good track in the target and UTC, an energy deposit in the B4 hodoscope consistent with an entering kaon and a delayed-coincidence of > 5 ns based on the $\check{C}_K$ and the IC. The acceptance of the range stack tracking cuts on the surviving $K_{\mu 2}$ events is given in second row of Table IV.

The acceptance of consistency of the range stack and

TABLE IV: Acceptance factors of the $K^+ \to \pi^+ \nu\bar{\nu}$ selection criteria measured with $K_{\mu 2}$ monitor trigger data. Only statistical uncertainties are shown. The product is $A_{K_{\mu 2}}$.

Cut	Acceptance factor
Range stack track reconstruction	0.99993 ± 0.00001
UTC-range stack track matching	0.99943 ± 0.00002
Beam and target pattern	0.15081 ± 0.00018
Photon veto	0.48122 ± 0.00200
$A_{K_{\mu 2}}$	0.07253 ± 0.00031

TABLE V: Acceptance factors measured with $K_{\pi 2}$ monitor trigger data. Uncertainties are statistical only. The product of all factors is $A_{K_{\pi 2}}$.

Cut	Acceptance factor
UTC reconstruction	0.94345 ± 0.00019
OPSVETO	0.97417 ± 0.00063
π^+ identification in target	0.71851 ± 0.00181
$A_{K_{\pi 2}}$	0.6604 ± 0.0018

UTC track was assessed using a $K_{\mu 2}$ sample with a good track in the range stack, a delayed-coincidence of > 5 ns based on the $\check{C}_K$ and the IC, and a single entering kaon selected based on the B4 energy deposit and the beam Čerenkov and wire chambers. The UTC-range stack track matching acceptance factor is given in the third row of Table IV.

The acceptance factor associated with the beam and target pattern recognition was evaluated on a sample of $K_{\mu 2}$ events that were required to have a single entering kaon and a good track in the UTC and range stack with $|\cos\theta| < 0.5$. In addition the momentum of the reconstructed track was required to be within two standard deviations of the expectation for $K_{\mu 2}$ decays. There were over forty individual cuts associated with the beam and target pattern recognition as described in Section III B 2. The majority of the individual cuts had acceptance greater than 90% except for the delayed-coincidence (75.5%) and the CCDPUL (45.1%) requirements. The fourth row of Table IV contains the overall acceptance factor of the beam and target cuts.

To measure the acceptance of the photon veto, an additional criterion was applied to the $K_{\mu 2}$ events used for the beam and target acceptance. As muons from $K_{\mu 2}$ decay can penetrate into the barrel veto, the reconstructed track was required to stop before the outermost layer of the range stack. The acceptance factor given in Table IV evaluated in this manner yielded the overall acceptance of both the online and offline photon veto cuts as the $K_{\mu 2}$ monitor trigger did not include the photon veto.

Acceptance factors from $K_{\pi 2}$ events

The $K_{\pi 2}$ monitor data was used to assess the acceptance factors associated with charged track reconstruction in the UTC and pion identification in the target. The acceptance of the veto of an additional track in the target (OPSVETO, Section III B 2) was measured with $K_{\pi 2}$ monitors. The factors are listed in Table V and described below.

To measure the acceptance of the UTC reconstruction, events from the $K_{\pi 2}$ monitor trigger were required to have a well-reconstructed track in the range stack and agreement between the online and offline determination of the range stack stopping counter. The factor is given in the second row of Table V.

For the measurement of the acceptance of the OPSVETO cut, in addition to the requirements described above, the charged track was required to be well-reconstructed in the UTC and range stack, identified as a

pion based on the measured range and momentum as well as the $\pi \to \mu \to e$ signature in the stopping counter and kinematically consistent with the pion from a $K_{\pi 2}$ decay. Cuts were also applied to ensure a single kaon entered the target. The acceptance factor for the OPSVETO is presented in the third row of Table V.

In addition to the requirements described above, the OPSVETO and target photon veto cuts were applied to the $K_{\pi 2}$ monitor events to assess the cumulative acceptance of the ten pion identification cuts in the target. These ten cuts were designed to reject tracks that contained an indication of a kink or discontinuity in the pattern of target fibers or target fibers with an unexpected energy deposit (Section III B 2). The acceptance factor for these cuts is listed in the fourth row of Table V. Two individual cuts with less than 90% acceptance were the requirement that no individual pion fiber had more than 3 MeV (89.6%) and the requirement on that the pattern of energy deposits in the target fibers was consistent with an unkinked pion trajectory (87.4%).

Acceptance factors from π_{scat} events

Beam pions that scatter in the target have a spectrum of range, energy and momentum similar to that of pions from $K^+ \to \pi^+ \nu\bar{\nu}$ and were used to determine the acceptance factors associated with the reconstruction and identification of pions in the range stack. Table VI lists the acceptance factors measured using π_{scat} monitors.

Candidate events were rejected if the pion stopped in a counter with a non-operational TD. The acceptance factor associated with this requirement was measured on a sample of π_{scat} monitor data selected by requiring a good outgoing track in the range stack, drift chamber, and target, a delayed-coincidence of less than 5 ns, a single pion entering the target and range, energy and momentum in the signal region. The acceptance factor is given in the second row of Table VI.

In addition to the requirements listed above, π_{scat} monitor data was also required to have a good $\pi \to \mu \to e$ signature and the pion was required to stop in range stack counter with an operational TD in order to measure the acceptance factor associated with the range stack kinematics and tracking. Assignment of target fibers to the incoming and outgoing pion in π_{scat} was not as robust as the assignments made for kaon decays at rest. Misassignment of target fibers yielded a larger uncertainty in the momentum, range and energy calculated for the outgoing pion in π_{scat} events. The effect of increasing or decreasing the signal phase space by ± 1 standard was used to estimate the systematic uncertainty in this acceptance factor that is shown in third row of Table VI.

The requirements used to assess the acceptance factor associated with a non-operational TD in the stopping counter were supplemented by requiring a good track in the drift chamber and range and momentum consistent with a pion in order to measure the acceptance factor associated with the $\pi \to \mu \to e$ signature. The cut on the measured dE/dx in range stack counters and the cuts on the consistency of the range stack and drift chamber

TABLE VI: Acceptance factors measured with π_{scat} monitor triggers. Operational is abbreviated as "Oper." The first and second uncertainties are statistical and systematic, respectively. The assessment of systematic uncertainties is described in the text. $A_{\pi_{\text{scat}}}$ is the product of the three acceptance factors.

Cut	Acceptance factor
Oper. TD in stopping counter	0.99843 ± 0.00010
Range stack kinematics	$0.82594 \pm 0.00126 \pm 0.01200$
$\pi \to \mu \to e$ signature	$0.4805 \pm 0.0015 \pm 0.0160$
$A_{\pi_{\text{scat}}}$	$0.3980 \pm 0.0014 \pm 0.0140$

TABLE VII: Acceptance factors determined from simulated $K^+ \to \pi^+ \nu \bar{\nu}$ decays. A_{MC} is the product of the three acceptance factors.

Component	Acceptance factor
Trigger	0.3225 ± 0.0015
Phase space	0.3650 ± 0.0027
π^+-nuclear interactions	0.8284 ± 0.0104
A_{MC}	0.0975 ± 0.0009

track had some correlation with the suite of cuts used to define the $\pi \to \mu \to e$ signature. The acceptance factor of the $\pi \to \mu \to e$ signature was assessed both with and without these cuts applied to estimate the systematic uncertainty due to these correlations. In addition a correction of 1.0% for pion decay-in-flight and pion absorption in the stopping counter, estimated from Monte Carlo, was applied to the acceptance factor given in the fourth row of Table VI.

Acceptance factors from simulated events

Simulated $K^+ \to \pi^+ \nu \bar{\nu}$ events were used to evaluate the trigger acceptance and the acceptance associated with phase space and π^+-nuclear interactions. The acceptance of the $L1.1$ and $L1.2$ (DC) components of the trigger as described in Section II were evaluated with $K_{\pi 2}$ ($K_{\mu 2}$) monitors as described previously in this Section. The acceptance of the remaining trigger components is given in the second row of Table VII. The phase space acceptance of the events surviving the trigger simulation is shown in the third row of the Table. The phase space acceptance includes the loss due to π^+ absorption and decay in flight. Neither the trigger or phase space acceptance include the effect of nuclear interactions. As indicated in Section III A, the combined trigger and phase space acceptance factor of 11.8% was larger than the corresponding factor of 6.5% for the $\pi \nu \bar{\nu}(1)$ region [1]. The acceptance factor associated with π^+-nuclear interactions was evaluated separately and is given in the fourth row of Table VII. For the $\pi \nu \bar{\nu}(1)$ region, the acceptance factor due to nuclear interactions was 49.5% [1].

Correction to the $T \cdot 2$ efficiency

The $T \cdot 2$ component of the trigger (Section II) required a coincidence between range stack counters in the same sector in the two innermost layers and in the IC. The simulation did not include the acceptance loss due to gaps between the neighboring T counters or due to insufficient

scintillation light in the thin T counters. These acceptance losses were measured by using $K_{\mu 2}$ and $K_{\pi 2}$ decays in KB monitor events. The energy loss in the T counter by the charged track differs for $K_{\mu 2}$ and $K_{\pi 2}$ events and simulated events were used to obtain the average energy loss for each decay. The measured acceptance factors for $K_{\mu 2}$ and $K_{\pi 2}$ were then extrapolated to estimate

$$A_{T \cdot 2} = 0.9505 \pm 0.0012 \pm 0.0143 \qquad (3)$$

where a $\pm 1.5\%$ systematic uncertainty was assigned to account for the extrapolation of the drift chamber track to the T counter.

Normalization to the $K_{\mu 2}$ branching ratio

We assessed the fraction (f_s) of K^+ that stopped in the target by normalization to the $K_{\mu 2}$ branching ratio [19] as described in [1]

$$f_s = 0.7740 \pm 0.0011 \quad . \qquad (4)$$

Confirmation of the $K_{\pi 2}$ branching ratio

We measured the $K_{\pi 2}$ branching fraction using the $K_{\pi 2}$ monitor trigger data in order to confirm the validity of the acceptance factors and corrections calculated with data and Monte Carlo. Our measurement followed the same analysis procedure as described in [1] but utilized the selection criteria developed for the pnn2 analysis. From this analysis we obtained

$$\mathcal{B}(K^+ \to \pi^+ \pi^0) = 0.221 \pm 0.002 \qquad (5)$$

where the uncertainty is statistical. This is in reasonable agreement with the world average value [19] of 0.209 ± 0.001 for the branching fraction.

Overall acceptance and sensitivity

The total acceptance was evaluated as the product of $A_{K_{\pi 2}}$, $A_{K_{\mu 2}}$, $A_{\pi_{\text{scat}}}$, A_{MC}, f_s and $A_{T \cdot 2}$ or $(1.37 \pm 0.14) \times 10^{-3}$ where we assigned a 10% uncertainty on the total acceptance to accomodate the discrepancy in $\mathcal{B}(K^+ \to \pi^+ \pi^0)$ and the additional systematic and statistical uncertainties in the acceptance evaluated in this Section. Based on the total exposure of 1.7×10^{12} stopped kaons for this analysis, the single event sensitivity (SES) of the $\pi \nu \bar{\nu}(2)$ analysis was SES $= (4.28 \pm 0.43) \times 10^{-10}$ which can be compared with the SES of the E949 $\pi \nu \bar{\nu}(1)$ analysis of $(2.55 \pm 0.20) \times 10^{-10}$ [1] and the combined SES of the previous $\pi \nu \bar{\nu}(2)$ analyses of $(6.87 \pm 0.04) \times 10^{-10}$ with the E787 apparatus [11, 18].

IV. RESULTS

In this Section, we describe the likelihood method used to evaluate the $K^+ \to \pi^+ \nu \bar{\nu}$ branching fraction and the results of examining the signal region. We also describe the evaluation of our observations within alternative models of $K^+ \to \pi^+$ nothing.

TABLE VIII: The estimated signal-to-background (s/b), background (b) and observed number of candidates for the nine cells. The cuts defining each cell are also given. The s/b is calculated assuming $\mathcal{B}(K^+ \to \pi^+\nu\bar{\nu}) = 1.73 \times 10^{-10}$. The uncertainties on b and s/b are omitted from the table. The definition column indicates the whether the tight version of the kinematics (KIN), photon veto (PV), delayed coincidence (DC) or $\pi \to \mu \to e$ (TD) cut or the inverted cut (*i.e.*, $\overline{\text{KIN}}$) was applied to define the cell. The cells containing signal candidate events A, B and C are indicated.

Cell definition	b	Candidates	s/b
$\text{KIN} \cdot \text{TD} \cdot \text{DC} \cdot \text{PV}$	0.152	0	0.84
$\text{KIN} \cdot \overline{\text{TD}} \cdot \text{DC} \cdot \text{PV}$	0.038	0	0.78
$\text{KIN} \cdot \text{TD} \cdot \overline{\text{DC}} \cdot \text{PV}$	0.019	0	0.66
$\text{KIN} \cdot \overline{\text{TD}} \cdot \overline{\text{DC}} \cdot \text{PV}$	0.005	0	0.57
$\text{KIN} \cdot \text{TD} \cdot \text{DC} \cdot \overline{\text{PV}}$	0.243	1 B	0.47
$\text{KIN} \cdot \overline{\text{TD}} \cdot \text{DC} \cdot \overline{\text{PV}}$	0.059	0	0.45
$\text{KIN} \cdot \text{TD} \cdot \overline{\text{DC}} \cdot \overline{\text{PV}}$	0.027	1 C	0.42
$\text{KIN} \cdot \overline{\text{TD}} \cdot \overline{\text{DC}} \cdot \overline{\text{PV}}$	0.007	0	0.35
$\overline{\text{KIN}}$	0.379	1 A	0.20

A. Likelihood method

We determined $\mathcal{B}(K^+ \to \pi^+\nu\bar{\nu})$ using a likelihood method that took into account the distributions of the predicted background and acceptance within the signal region. The signal region was divided into nine cells with differing acceptance-to-background ratios as described below. The likelihood ratio X was defined as

$$X \equiv \prod_{i=1}^{n} \frac{e^{-(s_i+b_i)}(s_i+b_i)^{d_i}}{d_i!} \Big/ \frac{e^{-b_i}b_i^{d_i}}{d_i!} \qquad (6)$$

where s_i and b_i were the estimated signal and background in the ith cell, d_i was the observed number of signal candidates in the ith cell and n was the total number of cells [25]. The estimated signal in each cell was given by $s_i \equiv \text{SES}_i \times \mathcal{B}(K^+ \to \pi^+\nu\bar{\nu})$ where SES_i was the single event sensitivity of the ith cell.

The division of signal region into nine cells was performed using combinations of the kinematics (KIN), photon veto (PV), delayed coincidence (DC) or $\pi \to \mu \to e$ (TD) cuts. We defined a standard and a more restrictive or "tight" version of each cut. The signal region was defined by the application of the standard version of all cuts. The signal region was then subdivided into cells by the additional selective application of the tight version of each cut or the inverted cut as shown in Table VIII.

The additional signal acceptance factor and rejection (Table IX) for each of the four tight cuts was determined using analogous techniques and samples as described in Section III D. Based on studies of data and simulated events, we assumed that the background components for which no rejection is given in the Table were reduced by the acceptance factor of the particular cut. For example, the acceptance of the cell defined by $\text{KIN} \cdot \overline{\text{TD}} \cdot \overline{\text{DC}} \cdot \text{PV}$ relative to the acceptance for the entire signal region was

TABLE IX: Additional acceptance factor (A) or rejection (R) for the tight version of the kinematics (KIN), photon veto (PV), delayed coincidence (DC) or $\pi \to \mu \to e$ (TD) cuts for specific backgrounds.

	KIN	TD	DC	PV
A	0.812	0.812	0.911	0.522
R	1.63 $(K_{\pi 2})$	3.08 (Muon)	6.3 (CEX)	2.75 $(K_{\pi 2(\gamma)})$
	2.70 (K_{e4})		1.0 (Beam)	
	1.20 $(K_{\pi 2\gamma})$			

TABLE X: Range, energy and momentum of the π^+ in the signal candidate events A, B and C as well as the measured K^+, π^+ and μ^+ lifetimes.

Candidate	A	B	C
Momentum (MeV/c)	161.5	188.4	191.3
Range (cm)	17.3	24.2	26.1
Kinetic energy (MeV)	76.1	95.6	97.9
K^+ lifetime (ns)	3.7	15.7	5.1
π^+ lifetime (ns)	22.4	16.7	10.2
μ^+ lifetime (ns)	5959.4	2270.6	9507.8

$A_{\text{KIN}} \times (1-A_{\text{TD}}) \times (1-A_{\text{DC}}) \times A_{\text{PV}}$ with obvious notation and the $K_{\pi 2}$-target-scatter background component relative to the contribution to the entire signal region was reduced by the factor $1/R_{\text{KIN}} \times (1-A_{\text{TD}}) \times (1-A_{\text{DC}}) \times 1/R_{\text{PV}}$.

B. Examination of the signal region

After completion of the background and acceptance analyses, all selection criteria were applied to the $\pi\nu\bar{\nu}(1+2)$ trigger data and three signal candidate events were selected. Some measured properties of the three events are listed in Table X and the cells containing candidates A, B and C are given in Table VIII. The kinetic energy *vs.* range of the three events along with the events found in the previous $\pi\nu\bar{\nu}(1)$ [1] and $\pi\nu\bar{\nu}(2)$ [11, 18] analyses are shown in Figure 10. The candidates's measured properties used in the selection criteria were consistent with the expected distributions for signal. There was no observed activity in the kaon fibers at the time of the π^+ for any of the three candidates according to the CCD-PUL analysis. The π^+ momentum of event A fails the KIN cut of 165 MeV/c. Events B and C fail the tight PV cut due to energy deposits of 2.4 and 2.1 MeV in the end cap above the 1.7 MeV threshold, respectively, and event C fails the tight DC cut of 6 ns on the kaon lifetime.

C. The $K^+ \to \pi^+\nu\bar{\nu}$ branching ratio

The central value of the $K^+ \to \pi^+\nu\bar{\nu}$ branching ratio was taken to be the value of $\mathcal{B}(K^+ \to \pi^+\nu\bar{\nu})$ that maximized X (Eqn 6) given the observed candidates. For the three events observed by this analysis, we determined $\mathcal{B}(K^+ \to \pi^+\nu\bar{\nu}) = (7.89^{+9.26}_{-5.10}) \times 10^{-10}$ where the quoted 68% confidence level interval was determined from the
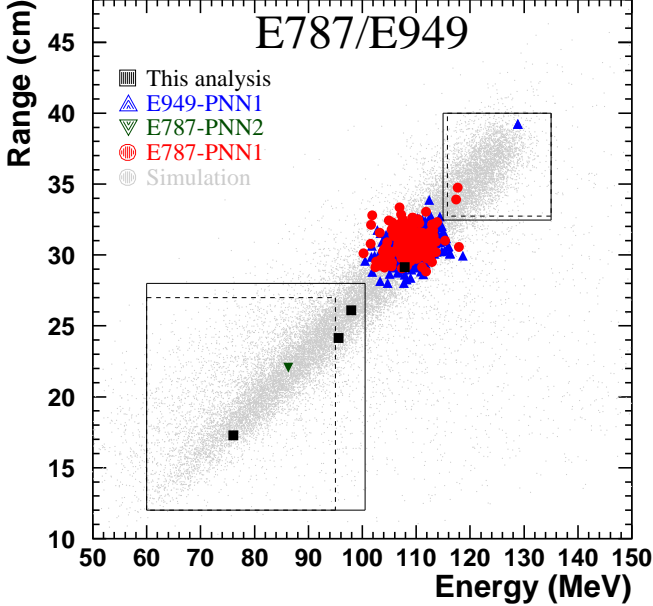
FIG. 10: Kinetic energy *vs.* range of all events passing all other cuts. The squares represent the events selected by this analysis. The circles and upward-pointing triangles represent the events selected by the E787 and E949 pnn1 analyses, respectively. The downward-pointing triangles represent the events selected by the E787 pnn2 analyses. The solid (dashed) lines represent the limits of the pnn1 and pnn2 signal regions for the E949 (E787) analyses. Despite the smaller signal region in E_π *vs.* R_π, the pnn1 analyses were 4.2 times more sensitive than the pnn2 analyses. The points near $E_\pi = 108$ MeV were $K_{\pi 2}$ decays that survived the photon veto cuts and were predominantly from the pnn1 analyses due to the higher sensitivity and the less stringent photon veto cuts. The light gray points are simulated $K^+ \to \pi^+ \nu\bar\nu$ events that would be accepted by our trigger.

behavior of X as described in [25] and took into account both the statistical and systematic uncertainties. The systematic uncertainties included the 10% uncertainty in the acceptance as well as the uncertainties in the estimation of the background components. The inclusion

of systematic uncertainties had a negligible effect on the confidence level interval due to the poor statistical precision inherent in a three event sample. The probability that these three events were due to background only, given the estimated background in each cell (Table VIII), was 0.037.

When the results of the previous $\pi\nu\bar\nu(1)$ and $\pi\nu\bar\nu(2)$ analyses [1, 11, 18] were combined with the results of this analysis, we found $\mathcal{B}(K^+ \to \pi^+\nu\bar\nu) = (1.73^{+1.15}_{-1.05}) \times 10^{-10}$. Systematic uncertainties were treated as described above when performing the combination, except that we assumed a correlated 10% un-

TABLE XI: The $K^+ \to \pi^+\nu\bar\nu$ branching ratio measurements in units of 10^{-10}. The prediction was taken from [26] and scaled to the two pion momentum regions using the standard model spectral shape for $K^+ \to \pi^+\nu\bar\nu$.

Momentum range (MeV/c)	Prediction	Measurement
[130, 205]	0.49 ± 0.04	$2.91^{+4.02}_{-1.79}$
[205, 227]	0.28 ± 0.02	$0.49^{+0.45}_{-0.29}$
All	0.85 ± 0.07	$1.73^{+1.15}_{-1.05}$

certainty for the acceptance assessed by each analysis. The probability that all seven events were due to background (background and standard model signal) was 0.001 (0.073).

The partial branching fraction for $K^+ \to \pi^+\nu\bar\nu$ for two pion momentum regions is given in Table XI along with the standard model prediction. The range of the two momentum regions is determined by the requirements on the reconstructed pion region and the detector resolution. The boundary between the two regions was determined by lower and upper limits on the reconstructed π^+ momentum that were set to be approximately 2.5 standard deviations from the nominal $K_{\pi 2}$ momentum for the $\pi\nu\bar\nu(1)$ and $\pi\nu\bar\nu(2)$ analyses, respectively. The lower limit of 130 MeV/c was also determined by $\pi\nu\bar\nu(2)$ requirement on the reconstructed pion momentum. The upper limit of 227 MeV/c is the kinematic limit for the $K^+ \to \pi^+\nu\bar\nu$ decay.

V. CONCLUSION

FIXME: TO BE WRITTEN

[1] S. Adler et al., Phys. Rev. **D77**, 052003 (2008), arXiv:0709.1000.

[2] A. J. Buras, F. Schwab, and S. Uhlig, Rev. Mod. Phys. **80**, 965 (2008), hep-ph/0405132.

[3] U. Camerini, D. Ljung, M. Sheaff, and D. Cline, Phys. Rev. Lett. **23**, 326 (1969).

[4] D. Ljung and D. Cline, Phys. Rev. **D8**, 1307 (1973).

[5] G. D. Cable, R. H. Hildebrand, C. Y. Pang, and R. Stiening, Phys. Rev. **D8**, 3807 (1973).

[6] M. S. Atiya et al., Phys. Rev. **D48**, 1 (1993).

[7] F. Mescia and C. Smith, Phys. Rev. **D76**, 034017 (2007), arXiv:0705.2025.

[8] J. Roy, Ph.D. thesis, University of British Columbia (1994).

[9] M. S. Atiya et al., Phys. Rev. Lett. **70**, 2521 (1993).

[10] S. S. Adler et al. (E787), Phys. Lett. **B537**, 211 (2002), hep-ex/0201037.

[11] S. Adler et al., Phys. Rev. **D70**, 037102 (2004), hep-

ex/0403034.

[12] B. Bhuyan, Ph.D. thesis, University of Delhi (2003).

[13] D. A. Bryman et al., Nucl. Instrum. Meth. **A396**, 394 (1997).

[14] M. Atiya, M. Ito, J. Haggerty, C. Ng, and F. W. Sippach, Nucl. Instrum. Meth. **A279**, 180 (1989).

[15] E. W. Blackmore et al., Nucl. Instrum. Meth. **A404**, 295 (1998).

[16] I. H. Chiang et al., IEEE Trans. Nucl. Sci. **42**, 394 (1995).

[17] T. K. Komatsubara et al., Nucl. Instrum. Meth. **A404**, 315 (1998).

[18] S. Adler et al., Phys. Lett. **B537**, 211 (2002), hep-ex/0201037.

[19] W. M. Yao et al., J. Phys. **G33**, 1 (2006).

[20] I.-A. Christidi, Ph.D. thesis, Stony Brook University (2006).

[21] K. Mizouchi, Ph.D. thesis, Kyoto University (2006).

[22] M. Ardebili, Ph.D. thesis, Princeton University (1995), UMI-95-27860.

[23] W. R. Nelson, H. Hirayama, and D. W. O. Rogers (1985), SLAC-0265.

[24] This method of assigning systematic uncertainty was intended to define a range that included the actual value of the background.

[25] T. Junk, Nucl. Instrum. Meth. **A434**, 435 (1999), hep-ex/9902006.

[26] J. Brod and M. Gorbahn, Phys. Rev. **D78**, 034006 (2008), arXiv:0805.4119. The uncertainty in the prediction is dominated by the uncertainty in the elements of the CKM matrix.